Journal of Fluids and Structures 17 (2003) 1–28

JOURNAL OF FLUIDS AND STRUCTURES

www.elsevier.nl/locate/jnlabr/yjfls

Estimation of the flutter derivatives of an NACA airfoil by means of Navier–Stokes simulation

O.P. Le Maître[a,*], R.H. Scanlan[b], O.M. Knio[c]

[a] *Centre d'Etudes de Mécanique d'Ile de France, Université d'Evry Val d'Essonne, 40 rue du Pelvoux-CE 140, 91020 Evry Cedex, France*
[b] *Department of Civil Engineering, The Johns Hopkins University, Baltimore, MD 21218-2686, USA*
[c] *Department of Mechanical Engineering, The Johns Hopkins University, North Charles-Street, Baltimore, MD 21218-2686, USA*

Received 23 August 2000; accepted 2 July 2002

Abstract

The paper presents a numerical determination of the aeroelastic characteristics of a two-dimensional airfoil. A numerical method is described for the resolution of the incompressible Navier–Stokes equations, based on a streamfunction/vorticity formulation in relative frame. The solution method employs influence matrix techniques to determine the exact boundary conditions and a conformal mapping of the physical space. Validation of the method is presented based on several test cases, and the code is then applied to the flutter derivatives of an airfoil. Two methodologies are tested for the calculation of the aerodynamics coefficients associated to the motion-related force functions proposed by Scanlan and Tomko. These are based on forced-motion and spring-mounted airfoil experiments. Results are compared with theoretical values based on the Theodorsen function. Good agreement with the inviscid theory is generally observed, except for the coefficients related to the angular velocity. The effects of the Reynolds number and the thickness of the airfoil are also investigated. The results indicate that, while the spring-mounted approach provides correct estimates of the flutter coefficients, the forced-motion approach is better suited for their computation.

1. Introduction

At the present time strong effort is being expended in the area of computational fluid dynamics. One problem of considerable practical interest is the estimation of time-varying fluid forces acting on oscillating bodies (Scanlan, 2000). A particular category of the test cases concerns two-dimensional (2-D) or along-wind "sectional" representations, as in the case of the well-known airfoil profile in a vibrating aircraft wing of infinite aspect ratio (Bisplighoff and Ashley, 1962). A parallel case is that of an along-wind section of a bridge of very long span (Scanlan and Tomko, 1971; Larsen and Walther, 1998; Beith, 1998). As one step toward eventual study of the bridge problem, and as a stand-alone exercise in methodology, the corresponding "classical" thin-airfoil problem is treated in this paper.

Because of the geometrical complications of actual bridge deck forms, it has been customary to test for their associated oscillatory aerodynamic coefficients in the wind tunnel rather than attempt to calculate them from first principles. Recent advances in computational fluid dynamics have, however, partially opened the door for the direct calculation of those associated aerodynamic oscillatory motion coefficients termed *flutter derivatives* (e.g., Deniz and

*Corresponding author. c/o Omar Knio, Department of Mechanical Engineering, The Johns Hopkins University, North Charles-Street, Baltimore, MD 21218-2686, USA.
E-mail address: olm@cemif.univ-evry.fr (O.P. Le Maître).

0889-9746/03/$ - see front matter
PII: S0889-9746(02)00111-1

Staubli, 1998; Larsen and Walther, 1998). This state of the art is exploited to a degree in the present paper, restricting the study, however, as a primary instance, to the flutter derivatives of a thin airfoil.

Specifically, the objective of the study described in this work is to obtain the motional aerodynamic coefficients, or flutter derivatives, of a thin airfoil undergoing oscillations within a smooth incompressible flow of medium-range Reynolds number. Consistent with the classical aeroelastic theory of flutter (Scanlan and Tomko, 1971), the flow in the present work is considered as 2-D. Numerical simulation of the flow is performed using a specially-design computational code that is based on a vorticity/streamfunction form of the Navier–Stokes equations. As described in Section 2, the method combines (i) a conformal mapping of the computational domain onto a rectangle (Theodorsen, 1931), which enables the use of an efficient solver for the resulting Poisson equation for the streamfunction; (ii) a systematic use of influence matrix techniques (see Vanel et al., 1986; Daube, 1992, Shen and Ta Phuoc, 1995) to determine the exact values of the streamfunction and the vorticity distribution along the airfoil surface, in a noniterative fashion; (iii) a multigrid algorithm (see McCormick, 1987) to solve the vorticity equation with good scalability properties with regard to the number of computational points; (iv) a procedure for the calculation of the fluid forces applied on the airfoil through a line integration along the airfoil surface; and (v) a coupling between airfoil and flow dynamics using a Newmark scheme (Zienkiewicz, 1977).

In Section 3, the formulation is generalized for a moving coordinate system attached to the body surface to handle moving airfoil problems, without requiring remeshing procedure. Then, in Section 4, the computation of the aerodynamic loads applied on the airfoil is detailed, together with the methodology accounting for coupling between the flow and the airfoil. The latter is considered in this context as a linear oscillator. In Section 5, we provide some results of test computations illustrating the efficiency and reliability of the method. These are demonstrated through comparison with measurements and other computations in the literature. In Section 6 the theory of flutter derivatives is presented, together with a discussion of two methodologies used for their extraction. The latter are based on simulations of forced-motion and spring-mounted airfoil experiments. These methods are applied in Sections 7 and 8, respectively, and the corresponding results are compared to each other as well as inviscid theoretical predictions. Major conclusions are summarized in Section 9.

2. Vorticity–Streamfunction Formulation

We are concerned with the solution of 2-D incompressible mass and momentum conservation equations, written in non-dimensional vorticity–streamfunction form as (Milne-Thomson, 1968; Vanel et al., 1986)

$$\frac{\partial\omega}{\partial t}+\nabla\cdot(\omega\boldsymbol{u})=\frac{1}{\mathrm{Re}}\nabla^2\omega, \tag{1}$$

$$\nabla^2\psi=-\omega. \tag{2}$$

Here, ω is the vorticity, ψ is the streamfunction, $\boldsymbol{u}=(u,v)=(\partial\psi/\partial y,-\partial\psi/\partial x)$ is the velocity vector, $\mathrm{Re}\equiv UL/\nu$ is the Reynolds number, U is the characteristic velocity, L characteristic length, and ν is the diffusivity. To ensure the equivalence of the (ψ,ω) formulation with the primitive Navier–Stokes equations, and because the domain is here simply connected, the following constraint arises:

$$\int_{\partial\Omega_o}\frac{\partial\omega}{\partial n}\,\mathrm{d}l=0, \tag{3}$$

where $\partial/\partial n$ denotes the normal derivative and $\partial\Omega_o$ the (stationary) airfoil surface. Eq. (3) shows that the net flux of vorticity entering the computational domain vanishes. This constraint is equivalent to enforcing the continuity of the pressure, p, around the obstacle.

2.1. Conformal mapping

In the following, we shall in particular consider the flow around an NACA0012 airfoil in an infinite domain. However, Eqs. (1) and (2) will be solved using finite difference techniques on a bounded domain. In order to use efficient fast solvers for the discrete set of equations, a coordinate transform is used that permits the treatment of the problem in a regular rectangular domain. In this work, we employ a conformal mapping that transforms a rectangular domain (X, Y) into physical space (x, y) around the airfoil. The transformation is defined as follows:

$$(X,Y)\in\left[0,\frac{\log R_\Gamma}{\pi}\right]\times[0,2]\to x+\mathrm{i}y=\exp\pi(X+\mathrm{i}\,Y)+B+\frac{C}{B+\exp\pi(X+\mathrm{i}\,Y)}, \tag{4}$$

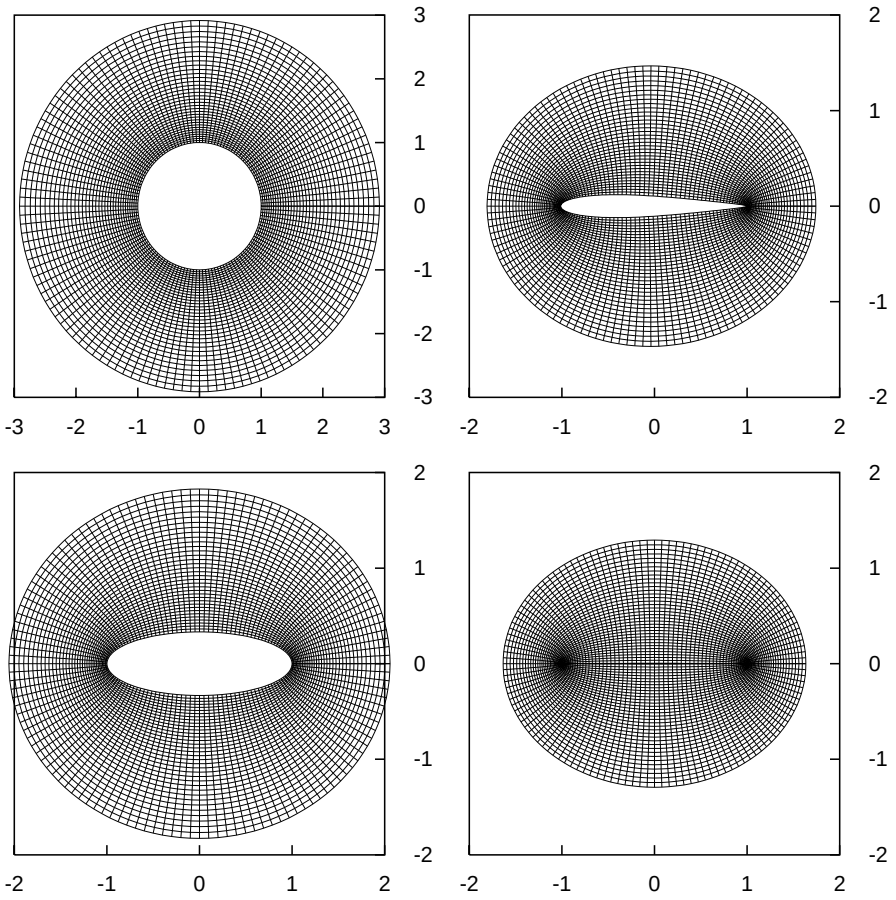

Fig. 1. Examples of different transformations of the mathematical plane onto the physical plane. Top left: $B = C = 0$ mapping of a cylinder. Top right: $B = -0.0647384$, $C = 0.8061$ mapping of an NACA0012 airfoil. Bottom left: $B = 0$, $C = 0.5$ mapping of an ellipse. Bottom right: $B = 0$, $C = 0.99$ mapping of a nearly flat plate.

where B and C are the transformation parameters. For an NACA0012 airfoil, $B = 0.647384$ and $C = 0.8061$. R_Γ gives the spatial extension of the computational domain around the airfoil. For $B = C = 0$, the transformation maps a circular domain, and for $B = 0$ and $C > 0$ one obtains a family of ellipses. Examples of transformations are given in Fig. 1.

In the transformed domain (X, Y), the governing equations are

$$\frac{\partial \omega}{\partial t} + \frac{1}{F}\tilde{\nabla} \cdot (\omega \tilde{\boldsymbol{u}}) = \frac{1}{F\,\mathrm{Re}}\tilde{\nabla}^2 \omega, \tag{5}$$

$$\tilde{\nabla}^2 \psi = -F\omega, \tag{6}$$

where

$$F \equiv \left| \frac{\mathrm{d}(x + \mathrm{i}y)}{\mathrm{d}(X + \mathrm{i}Y)} \right| \tag{7}$$

is the modulus of the transformation and $\tilde{\boldsymbol{u}} \equiv (\partial\psi/\partial Y, -\partial\psi/\partial X)$.

In the mathematical domain, constraint (3) is expressed as

$$\int_0^2 \left. \frac{\partial \omega}{\partial X} \right|_{X=0} \mathrm{d}\,Y = 0. \tag{8}$$

The boundary conditions and solution methods are now detailed.

2.2. External boundary conditions

To solve the governing equations one has to provide boundary conditions for ψ and ω, on the obstacle as well as on far boundaries, denoted by $\partial\Omega_o$ and $\partial\Omega_\Gamma$. In the transformed domain, these correspond to $X=0$ and $X=\frac{1}{\pi}\log R_\Gamma$, respectively. For the computations presented below, the computational domain extends far from the obstacle (typically, $R_\Gamma=80$), so that we can approximate the value of ψ on $\partial\Omega_\Gamma$ to be equal to the undisturbed streamfunction of the incoming flow:

$$\psi_\Gamma=\psi((x,y)\in\partial\Omega_\Gamma)=\psi_\infty(x,y)=U_\infty y-V_\infty x, \tag{9}$$

with U_∞ and V_∞ the free-stream velocity components. In so doing, we impose the flow rate in the computational domain.

For the ω boundary values, two different conditions have been tested: (i) homogeneous Dirichlet boundary condition: $\omega_\Gamma=\omega((x,y)\in\Omega_\Gamma)=0$, which assumes that the external boundary is so far from the obstacle that one can consider that vortices have completely diffused if/when they reach the external boundary; (ii) inflow/outflow boundary condition: the value of ω_Γ on $\partial\Omega_\Gamma$ is estimated through an explicit integration of the convective part of Eq. (1) on the portions of $\partial\Omega_\Gamma$ where the convective flux leaves the computational domain, elsewhere, the homogeneous Dirichlet boundary condition is applied. Numerical tests have shown very little dependence of the computed solutions upon the kind of boundary external conditions selected on $\partial\Omega_\Gamma$. We now focus on boundary conditions on the obstacle.

2.3. Wall boundary conditions

The system of equations to be solved, together with boundary conditions, is

$$\frac{\partial\omega}{\partial t}+\frac{1}{F}\tilde{\nabla}\cdot(\omega\tilde{\boldsymbol{u}})=\frac{1}{F\,\mathrm{Re}}\tilde{\nabla}^2\omega, \tag{10a}$$

$$\tilde{\nabla}^2\psi=-\omega F, \tag{10b}$$

$$\tilde{\boldsymbol{u}}=\left(\frac{\partial\psi}{\partial Y},-\frac{\partial\psi}{\partial X}\right), \tag{10c}$$

$$\psi=\psi_\Gamma,\ \omega=\omega_\Gamma\ \text{on}\ \Omega_\Gamma,\ \tilde{\boldsymbol{u}}=0\ \text{on}\ \Omega_o, \tag{10d}$$

$$\int_0^2\left.\frac{\partial\omega}{\partial X}\right|_{X=0}\mathrm{d}Y=0, \tag{10e}$$

where the determination of ψ_Γ and ω_Γ has been discussed in the previous subsection. Introducing a second order discretization of the time derivative appearing in Eqs. (10), and an explicit estimation of the nonlinear terms, one obtains the following semi-discrete form of Eqn. (10)):

$$(\sigma-\tilde{\nabla}^2)\omega^{n+1}=f^{n+1}\equiv\frac{F\,\mathrm{Re}}{2\Delta t}(4\omega^n-\omega^{n-1})-\mathrm{Re}\,\tilde{\nabla}\cdot\left[(2\omega\tilde{\boldsymbol{u}})^n-(\omega\tilde{\boldsymbol{u}})^{n-1}\right], \tag{11}$$

where $\sigma=3F\,\mathrm{Re}/2\Delta t$, Δt is the time step, while the superscript refers to the time level. One of the difficulties in the solution of the above equation is that the natural boundary conditions on a fixed wall are no-slip velocity, i.e., $\tilde{\boldsymbol{u}}=0$, which does not directly provide values of the wall vorticity, $\omega_o=\omega((x,y)\in\Omega_o)$. In addition, by treating the obstacle as a streamline, one concludes that $\psi_o=\psi((x,y)\in\Omega_o)$ is constant; however, the value of this constant is not explicitly known, but is obtained from the pressure continuity constraint, Eq. (3). Thus, the solution of the Helmholtz equation in (11) is coupled to that of the streamfunction Poisson equation (10)). In order to address these difficulties, and in the process decouple these two elliptic problems, we have adopted the influence matrix technique proposed by Daube (1992) (see also Worlibar et al., 1998). Specific details on this approach are omitted.

2.4. Discretization and solvers

Numerical simulation of the governing equations is based on a finite-difference methodology (see Fletcher, 1988). In the transform plane, the computational domain consists of the rectangle $[0,\log(R_\Gamma)/\pi]\times[0,2]$. Variables are represented at the nodes of a computational grid which is used to discretize the domain. A uniform Cartesian grid with (NX,NY) points in the (X,Y) direction is used for this purpose. Second-order centered differences are used to discretize

all spatial derivatives, except for the convective vorticity terms which are treated using Leonard's third-order upwind scheme (see Tamura et al., 1990).

Discretization of the streamfunction–vorticity Poisson equation leads to a linear system of equations which must be inverted at every time step. In order to solve the system efficiently, we exploit the periodicity in the Y direction and construct a discrete Fourier representation of the vorticity and streamfunction values (Buzbee et al., 1970). This transforms the original discretized system into a decoupled collection of NY 1-D problems involving the streamfunction and vorticity Fourier coefficients. These 1-D systems are governed by system matrices with a tri-diagonal structure, and are efficiently inverted with $O(NX)$ scheme. Thus, inversion of the complete system is performed in essentially $O(NXNY)$ computations.

The implicit treatment of the viscous terms in the vorticity transport equation also leads to a linear system of equations. In this discrete Helmholtz system, however, the presence of a Y-varying Jacobian function F complicates the implementation of a Fourier-based representation, as diagonalization is no longer possible. Consequently, an alternative iterative multigrid technique is considered (Mc Cormick, 1987). The multigrid technique uses $k_{\max}$ refinement levels, where the finest grid coincides with the computational grid defined above. Coarser levels are defined by successively halving the number of grid points. At every grid level k, 3^k Gauss–Seidel iterations are performed in order to reduce the residual, and V-cycles are repeated until the residual on the finest grid falls below a predefined tolerance ε. In the computations below, we use $\varepsilon = 10^{-7}$, and we find that 1–6 V-cycles are needed to reduce the residual below this level.

3. Moving airfoil

We now consider the case of a moving airfoil placed in a steady, uniform stream with far-field velocity $\boldsymbol{u}_\infty = (U_\infty, V_\infty)$. The displacement of the airfoil is described through its instantaneous rotation rate $\Omega_a(t)$ around a given center of rotation $\boldsymbol{X}_R(t)$ and by its translation velocity vector $\boldsymbol{U}_a(t) = (u_a, v_a)$.

Let $\boldsymbol{X}_B(t)$ denote the center of mass of the airfoil. The instantaneous velocity of the center of mass obeys

$$\frac{\mathrm{d}\boldsymbol{X}_B}{\mathrm{d}t} = \boldsymbol{U}_a + \Omega_a \boldsymbol{k} \wedge (\boldsymbol{X}_B - \boldsymbol{X}_R). \tag{12}$$

We will denote by $\boldsymbol{X}^a$ the coordinate vector in the laboratory or absolute reference frame, and by $\boldsymbol{X}^r$ the coordinate vector in the reference frame attached to the body (see Fig. 2). Thus, a fixed point $\boldsymbol{x} = (x, y)$ in the relative frame has absolute velocity $\boldsymbol{U}_a + \Omega_a \boldsymbol{k} \wedge (\boldsymbol{x} - \boldsymbol{X}_R)$.

A convenient streamfunction–vorticity formulation of the problem in the relative frame is given by

$$\frac{\partial \omega_a}{\partial t} + \nabla \cdot [\omega_a \boldsymbol{u}_r] = \frac{1}{\mathrm{Re}} \nabla^2 \omega_a, \tag{13a}$$

$$\nabla^2 \psi_r = -\omega_a + 2\Omega_a, \tag{13b}$$

$$\boldsymbol{u}_r = \nabla \wedge (\psi_r \boldsymbol{k}), \tag{13c}$$

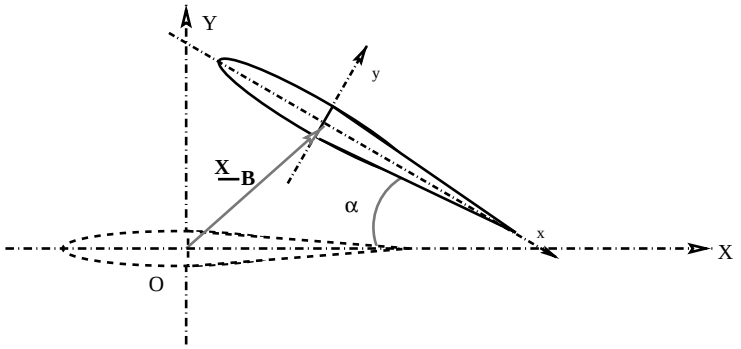

Fig. 2. Description of the notations used for the formulation in relative frame. The reference frame is (O, X, Y). The obstacle is located by the position of its center $\boldsymbol{X}_B$ and the rotation angle α, which also corresponds to the angle of attack. The instantaneous rate of rotation is $\mathrm{d}\alpha/\mathrm{d}t = \Omega_a(t)$.

where ω_a is the absolute vorticity, ψ_a and ψ_r are the absolute and relative streamfunctions, respectively, and u_r is the relative velocity. The relative streamfunction is related to the absolute streamfunction through

$$\nabla \wedge (\psi_r \boldsymbol{k}) = \nabla \wedge (\psi_a \boldsymbol{k}) - \Omega_a \boldsymbol{k} \wedge (\boldsymbol{x} - \boldsymbol{X}_R) - \boldsymbol{U}_a, \tag{14}$$

while the relative and absolute velocities are related by

$$\boldsymbol{u} = \boldsymbol{U}_a(t) + \boldsymbol{u}_r + \Omega_a \boldsymbol{k} \wedge (\boldsymbol{x} - \boldsymbol{X}_R). \tag{15}$$

The governing system (13) is subject to the following conditions or constraints:

$$\begin{aligned} &\boldsymbol{u}_r = 0 && \text{on } \partial\Omega_o, \\ &\psi_r = [\boldsymbol{U}_\infty \wedge \boldsymbol{x} - \boldsymbol{U}_a \wedge \boldsymbol{x} - (\Omega_a \boldsymbol{k} \wedge (\boldsymbol{x} - \boldsymbol{X}_R)) \wedge (\boldsymbol{x} - \boldsymbol{X}_R)] \cdot \boldsymbol{k} && \text{on } \partial\Omega_\Gamma, \\ &\frac{1}{\mathrm{Re}} \int_0^2 \left. \frac{\partial \omega_a}{\partial X} \right|_{X=0} \mathrm{d}Y = - \int_0^2 \left. \frac{\mathrm{d}(\Omega_a \wedge (\boldsymbol{x} - \boldsymbol{X}_R))}{\mathrm{d}t} \right|_{X=0} \wedge \boldsymbol{n} \sqrt{F}\, \mathrm{d}Y, && \end{aligned} \tag{16}$$

and suitable vorticity conditions on $\partial\Omega_\Gamma$.

The methodology of Section 2 still applies, with minor differences which are now listed. First, the problem accounts for the rotation of the relative frame by adding the $2\Omega_a$ term on the right-hand side of the Poisson equation. Second, the external boundary condition on the streamfunction, given in Eq. (16), accounts for the translations and rotation of the reference frame. Finally, the dynamic integral constraint in Eq. (16) now represents the balance between the net flux of vorticity entering in the fluid domain as well the time derivative of the circulation on $\partial\Omega_o$.

4. Fluid forces and airfoil dynamics

In order to determine the motion of the airfoil, the fluid forces applied on the body must be estimated. When these are known, the displacement of the airfoil is obtained by integrating the equations of motion describing its dynamics. In this section we describe the determination of the fluid forces, the equations of motion of the airfoil, and the coupling between the flow and airfoil dynamics.

In doing so we shall rely on the notations illustrated in Fig. 3. Specifically, we introduce the local basis $(\boldsymbol{n}, \boldsymbol{\tau})$ in the physical domain, where $\boldsymbol{n}$ and $\boldsymbol{\tau}$ respectively denote the unit vectors tangential to the transformed constant X and constant Y lines in the mathematical domain. By virtue of the conformal mapping, this basis is orthogonal. Moreover, $\partial/\partial n$ and $\partial/\partial\tau$ refer to differentiation in the directions $\boldsymbol{n}$ and $\boldsymbol{\tau}$ in the physical domain. Thus, u_n and u_τ denote the components of the velocity expressed in the basis $(\boldsymbol{n}, \boldsymbol{\tau})$, i.e., $\boldsymbol{u} = u_n \boldsymbol{n} + u_\tau \boldsymbol{\tau}$.

4.1. Pressure distribution

To determine the pressure distribution on the airfoil, we start from the momentum equation in the absolute reference frame:

$$\boldsymbol{\Gamma} + \nabla p = \frac{1}{\mathrm{Re}} \nabla^2 \boldsymbol{U}, \tag{17}$$

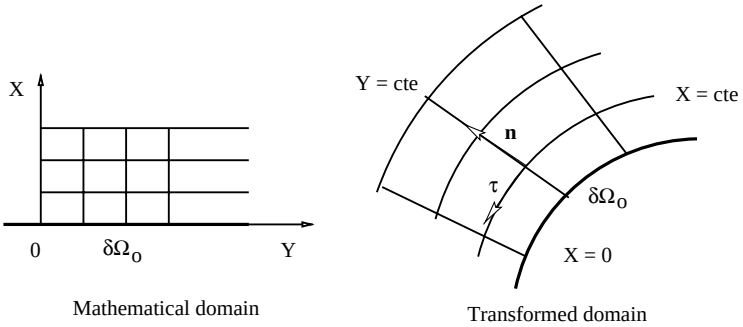

Fig. 3. Notation used in Section 4. The local basis $(\boldsymbol{n}, \boldsymbol{\tau})$ of the physical space is orthonormal. The vector $\boldsymbol{n}$ is tangential to the constant Y lines, while $\boldsymbol{\tau}$ is tangential to the constant X lines.

where $\mathbf{\Gamma} \equiv \mathrm{D}\boldsymbol{u}/\mathrm{D}t$ is the material acceleration. By taking the scalar product of Eq. (17) with $\boldsymbol{\tau}$, and expressing the viscous force in terms of relative velocity, we get

$$\frac{\partial p}{\partial \tau} = -\mathbf{\Gamma}(\boldsymbol{x}) \cdot \boldsymbol{\tau} + \frac{1}{\mathrm{Re}} \frac{\partial \omega_r}{\partial n}, \tag{18}$$

where $\omega_r \equiv \omega_a - \Omega_a$ is the relative vorticity. The pressure distribution on the solid boundary is obtained by integration of Eq. (18), i.e.

$$p(\tau) = p(0) + \int_0^\tau \left[-\mathbf{\Gamma} \cdot \boldsymbol{\tau} + \frac{1}{\mathrm{Re}} \frac{\partial \omega_r}{\partial n} \right] \mathrm{d}\tau', \tag{19}$$

where $p(0)$ is an arbitrary constant.

4.2. Distribution of Viscous Stresses

Following the present notation conventions, the viscous stress tensor on the boundary $\partial\Omega_o$ is expressed as

$$\bar{\boldsymbol{\sigma}} = \frac{1}{\mathrm{Re}} \begin{pmatrix} \dfrac{\partial u_n}{\partial n} & 0 \\ \dfrac{\partial u_\tau}{\partial n} & \dfrac{\partial u_\tau}{\partial \tau} \end{pmatrix}, \tag{20}$$

where we have used the continuity equation

$$\nabla \cdot \boldsymbol{u}_r = \frac{\partial v_\tau}{\partial \tau} + \frac{\partial v_n}{\partial n} = 0 \tag{21}$$

to conclude that the normal derivative of $\boldsymbol{n}$ vanishes on the boundary, i.e., $\partial v_n/\partial n = 0$ on $\partial\Omega_o$. The tangential viscous stress at the boundary, $\boldsymbol{S}$, is thus given by

$$\boldsymbol{S} = \bar{\boldsymbol{\sigma}} \cdot \boldsymbol{n} = \frac{\omega_r}{\mathrm{Re}} \boldsymbol{\tau}. \tag{22}$$

4.3. Airfoil dynamics

Similar to the system configuration in Scanlan and Tomko (1971), we consider a 2-D airfoil with two degrees of freedom: a vertical translation and a rotation around its center of mass. The deviations from the rest position will be denoted respectively by h for the translation distance and α for the rotation angle. We also assume that the configuration $\alpha = 0$ corresponds to a null angle of attack relative to the free stream, and that the airfoil is balanced so that its center of mass coincides with its center of rotation. The motion of the airfoil is governed by the following system:

$$m\left[\ddot{h} + 2\omega_h \xi_h \dot{h} + \omega_h^2 h\right] = \frac{\rho V_\infty^2 B}{2} C_L(t), I\left[\ddot{\alpha} + 2\omega_\alpha \xi_\alpha \dot{\alpha} + \omega_\alpha^2 \alpha\right] = \frac{\rho V_\infty^2 B^2}{2} C_T(t), \tag{23}$$

where m and I are the mass and mass moment of inertia per unit length of span, respectively; ξ_h and ξ_α are damping ratios in bending and torsion, respectively; ω_h and ω_α are the natural mechanical frequencies; V_∞ is the dimensional velocity of the freestream; B is the chord length of the airfoil; ρ is the fluid density; and C_L and C_T are the instantaneous aerodynamic lift and torque coefficients, respectively. The dots and double dots are used to denote first and second time derivatives.

Based on the notation introduced in Section 3, we have the following relationships between α, $\dot{\alpha}$, $\ddot{\alpha}$ and Ω_a, $\mathrm{d}\Omega_a/\mathrm{d}t$, $\boldsymbol{u}_\infty$:

$$\Omega_a = \dot{\alpha},$$

$$\frac{\mathrm{d}\Omega_a}{\mathrm{d}t} = \ddot{\alpha}, \tag{24}$$

$$\boldsymbol{u}_\infty = \begin{pmatrix} \cos\alpha \\ -\sin\alpha \end{pmatrix}.$$

Letting $\boldsymbol{D}$ denote the vector describing the state of the airfoil, i.e.,

$$\boldsymbol{D} \equiv \begin{pmatrix} h \\ \alpha \end{pmatrix}, \tag{25}$$

we can rewrite Eqn. (23) in matrix form as

$$\begin{bmatrix} m\omega_h^2 & 0 & 2m\xi_h\omega_h & 0 & m & 0 \\ 0 & I\omega_\alpha^2 & 0 & 2I\xi_\alpha\omega_\alpha & 0 & I \end{bmatrix} \begin{pmatrix} \boldsymbol{D} \\ \dot{\boldsymbol{D}} \\ \ddot{\boldsymbol{D}} \end{pmatrix} = \frac{\rho V_\infty^2 B}{2} \begin{pmatrix} C_L(t) \\ BC_T(t) \end{pmatrix}. \tag{26}$$

In the computations, the evolution of D is numerically obtained using a Newmark scheme (Zienkiewicz, 1977); we have

$$\begin{aligned} \boldsymbol{D}^{n+1} &= \boldsymbol{D}^n + \Delta t_s \dot{\boldsymbol{D}}^n + (0.5-\theta)\Delta t_s^2 \ddot{\boldsymbol{D}}^n + \theta \Delta t_s^2 \ddot{\boldsymbol{D}}^{n+1}, \\ \dot{\boldsymbol{D}}^{n+1} &= \dot{\boldsymbol{D}}^n + (1-\mu)\Delta t_s \ddot{\boldsymbol{D}}^n + \mu \Delta t_s \ddot{\boldsymbol{D}}^{n+1}, \end{aligned} \tag{27}$$

where superscripts are used to denote the time level, Δt_s is the time step, and μ, θ are numerical integration parameters. For $\mu = \theta = 0$ we recover the classical Euler forward scheme, while for $\mu = 1$ and $\theta = 0.5$ we have the Euler backward scheme. Combining the present discretization scheme with Eq. (26), we obtain

$$\begin{pmatrix} \boldsymbol{D}^{n+1} \\ \dot{\boldsymbol{D}}^{n+1} \\ \ddot{\boldsymbol{D}}^{n+1} \end{pmatrix} = [K]^{-1} \begin{pmatrix} \boldsymbol{D}^n + \Delta t_s \dot{\boldsymbol{D}}^n + (0.5-\theta)\Delta t_s^2 \ddot{\boldsymbol{D}}^n \\ \dot{\boldsymbol{D}}^n + (1-\mu)\Delta t_s \ddot{\boldsymbol{D}}^n \\ \overline{\boldsymbol{F}}^n \end{pmatrix}, \tag{28}$$

where

$$\overline{\boldsymbol{F}}^n \equiv \frac{\rho V_\infty^2 B}{2} \begin{pmatrix} C_L^n \\ BC_T^n \end{pmatrix} \tag{29}$$

is the fluid load vector and

$$[K] = \begin{bmatrix} 1 & 0 & 0 & 0 & -\theta\Delta t_s^2 & 0 \\ 0 & 1 & 0 & 0 & 0 & -\theta\Delta t_s^2 \\ 0 & 0 & 1 & 0 & -\mu\Delta t_s & 0 \\ 0 & 0 & 0 & 1 & 0 & -\mu\Delta t_s \\ m\omega_h^2 & 0 & 2m\xi_h\omega_h & 0 & m & 0 \\ 0 & I\omega_\alpha^2 & 0 & 2I\xi_\alpha\omega_\alpha & 0 & I \end{bmatrix}. \tag{30}$$

The lift and torque coefficients are obtained by integrating the pressure and viscous stress distributions along the body surface. Let $\boldsymbol{F}$ and T denote the total fluid force and fluid torque relative to the center of rotation X_R, respectively. In the relative reference frame and with respect to the basis $(\boldsymbol{n}, \boldsymbol{\tau})$, we have

$$\boldsymbol{F} = \int_{\partial\Omega_o} \left[\frac{\omega_r}{\mathrm{Re}} \boldsymbol{\tau} - p(\tau)\boldsymbol{n} \right] \mathrm{d}\tau \tag{31}$$

and

$$T = \int_{\partial\Omega_o} \left[\frac{\omega_r}{\mathrm{Re}} (\boldsymbol{x} - \boldsymbol{X}_R) \wedge \boldsymbol{\tau} - p(\tau)(\boldsymbol{x} - \boldsymbol{X}_R) \wedge \boldsymbol{n} \right] \mathrm{d}\tau. \tag{32}$$

Consequently, the lift and torque coefficients are given by

$$C_L = (\boldsymbol{F} \wedge \tilde{\boldsymbol{u}}_\infty) \cdot \boldsymbol{k} \tag{33}$$

and

$$C_T = \int_{\partial\Omega_o} \left[\frac{\omega_r}{\mathrm{Re}} (\boldsymbol{x} - \boldsymbol{X}_R) \wedge \boldsymbol{\tau} - p(\tau)(\boldsymbol{x} - \boldsymbol{X}_R) \wedge \boldsymbol{n} \right] \mathrm{d}\tau \tag{34}$$

respectively. Meanwhile, the drag coefficient is defined by

$$C_D \equiv \boldsymbol{F} \cdot \tilde{\boldsymbol{u}}_\infty . \tag{35}$$

4.4. Normalization and coupling

In order to couple the equations of motion of the airfoil and fluid a consistent normalization convention is required. Normalization of the governing equations for the fluid is based on selecting the free-stream velocity V_∞ as characteristic velocity scale, and the half-cord $B/2$ as characteristic lengthscale. This results in characteristic time scale $t^* \equiv B/(2V_\infty)$. Under this normalization convention, the equations of motion of the airfoil are expressed as

$$\begin{pmatrix} \boldsymbol{D}^{n+1} \\ \dot{\boldsymbol{D}}^{n+1} \\ \ddot{\boldsymbol{D}}^{n+1} \end{pmatrix} = [K^*]^{-1} \begin{pmatrix} \boldsymbol{D}^n + \Delta t \dot{\boldsymbol{D}}^n + (0.5 - \theta)\Delta t^2 \ddot{\boldsymbol{D}}^n \\ \dot{\boldsymbol{D}}^n + (1 - \mu)\Delta t \ddot{\boldsymbol{D}}^n \\ \overline{\boldsymbol{F}}^n \end{pmatrix}, \tag{36}$$

where the normalized stiffness matrix $[K^*]$ is given by

$$[K^*] = \begin{bmatrix} 1 & 0 & 0 & 0 & -\theta\Delta t^2 & 0 \\ 0 & 1 & 0 & 0 & 0 & -\theta\Delta t^2 \\ 0 & 0 & 1 & 0 & -\mu\Delta t & 0 \\ 0 & 0 & 0 & 1 & 0 & -\mu\Delta t \\ m\omega_h^2 & 0 & 2\dfrac{m}{t^*}\xi_h\omega_h & 0 & \dfrac{m}{t^{*2}} & 0 \\ 0 & I\omega_\alpha^2 & 0 & 2\dfrac{I}{t^*}\xi_\alpha\omega_\alpha & 0 & \dfrac{I}{t^{*2}} \end{bmatrix}. \tag{37}$$

In light of the structure of the stiffness matrix $[K^*]$, it is clear that coupling between the displacement (h) and rotation (α) can only occur through the fluid force term $\overline{\boldsymbol{F}}$. In addition, if one wishes to constrain one of these degrees of freedom, it suffices to set to zero the corresponding fluid force term in $\overline{\boldsymbol{F}}$. Also note that for the parameter regime considered in the present study, the simple staggered coupling scheme provides stable and accurate solutions, as shown in the examples below.

5. Validation

Before applying the numerical codes to the study of flutter derivatives, tests are performed in this section in order to verify the predictions. To this end, the codes are used to compute the unsteady flow field around a stationary cylinder, a spinning cylinder, a stationary airfoil at large angle of attack, and an oscillating airfoil. Computed predictions are then compared with published experimental or computational data.

5.1. Flow around a fixed cylinder

The flow around a stationary cylinder has been extensively analyzed and many suitable references are available for the purpose of comparison. In this section we consider two test cases, based on (a) the early stages of the flow around an impulsively started cylinder and (b) the stationary unsteady field that is established at large times after the loss of symmetry in the cylinder wake.

The impulsively started motion around a circular cylinder is computed for a Reynolds number $\mathrm{Re} = 3000$. Variables are normalized with respect to the appropriate combination of the fluid density, the free-stream velocity, and the cylinder radius. The simulation is performed by setting to zero the parameters B and C of the conformal transformation. The computational domain has $R_\Gamma = 50$, and is discretized using a grid with $NX = 200$ and $NY = 160$. The normalized integration time step $\Delta t = 0.005$.

Fig. 4 shows instantaneous streamfunction and vorticity contours at dimensionless times $t = 1$, 2, 4, and 6 after the impulsive start. The plots clearly depict the growth of the boundary layer, as well as the formation of a symmetric pair of vortices in the wake of the cylinder. In order to test the predictions, we compare in Fig. 5 the computed streamwise velocity component along the axis of symmetry in the near wake with the experimental measurements of Loc and Bouard (1985). The experimental and computed profiles exhibit a similar time evolution but a time shift is evident between the two. Similar phase shifts have also been reported in other numerical studies (e.g., Chang and Chern, 1991). The test may nonetheless be considered satisfactory.

Due to the essential instability of the cylinder wake, the flow loses its symmetry and a von Karman vortex street is established behind the cylinder, as shown in Fig. 6. A stationary regime is eventually reached in which the flow is dominated by the periodic shedding of opposite-sign vortices in the cylinder wake. Computations are performed in order to examine the properties of the stationary flow. Results are obtained for two Reynolds numbers, $\mathrm{Re} = 200$ and 855. Fig. 7 shows the time evolution of the lift and drag coefficients, respectively,

$$C_L \equiv \frac{F_L}{0.5\rho U_\infty^2 D} \tag{38}$$

and

$$C_D \equiv \frac{F_D}{0.5\rho U_\infty^2 D}. \tag{39}$$

Here, F_L denotes the lift force per unit depth, F_D denotes the drag force per unit depth, and D is the diameter of the cylinder. As expected, the instantaneous lift and drag coefficients exhibit an oscillatory behavior with well-defined frequencies. The computed predictions are compared in Table 1 with experimentally determined and computed values (Zang and Dalton, 1997; Lecointe and Picquet, 1989). The comparison shows that the computations are in good agreement with the measurements and the other numerical results.

5.2. Rotating cylinder in uniform flow

In order to test the formulation and computations in a relative frame of motion (Section 3), we consider the problem of a circular cylinder rotating around its center at a constant angular velocity Ω_a, while placed in a uniform and constant free stream U_∞. Again, two studies are performed: the first focuses on the flow developing after the impulsively started motion, while the second focuses on the characteristics of the periodic state at larger times. This problem has two parameters which are the Reynolds number based on the free-stream velocity, and the dimensionless velocity Vr defined as the ratio of the velocity on the cylinder boundary to the inflow velocity:

$$V_r \equiv \frac{\Omega_a R}{U_\infty}. \tag{40}$$

The early stages of the flow have been studied by Bard and Dennis (1985) and Bard et al. (1989). In our computations, the cylinder cannot be set impulsively into rotation in order to control the vorticity released into the fluid. Thus, we approximate the impulsive start using a short-duration transient phase during which the acceleration decreases linearly with time to vanish for $t \geqslant t_s$. In the present computations, we use $t_s = 0.1$. As in the previous section, variables are normalized with respect to the appropriate combination of the fluid density, the free-stream velocity, and the cylinder radius.

Fig. 8 compares the unsteady evolution of the computed lift, drag, and torque coefficients, together with some data-points extracted from Bard and Dennis (1985). In the two computations, the Reynolds number $\mathrm{Re} = 200$ and the velocity ratio $V_r = 1$. Our computations are performed using a time step $\Delta t = 0.01$ and a domain with $R_\Gamma = 30$,

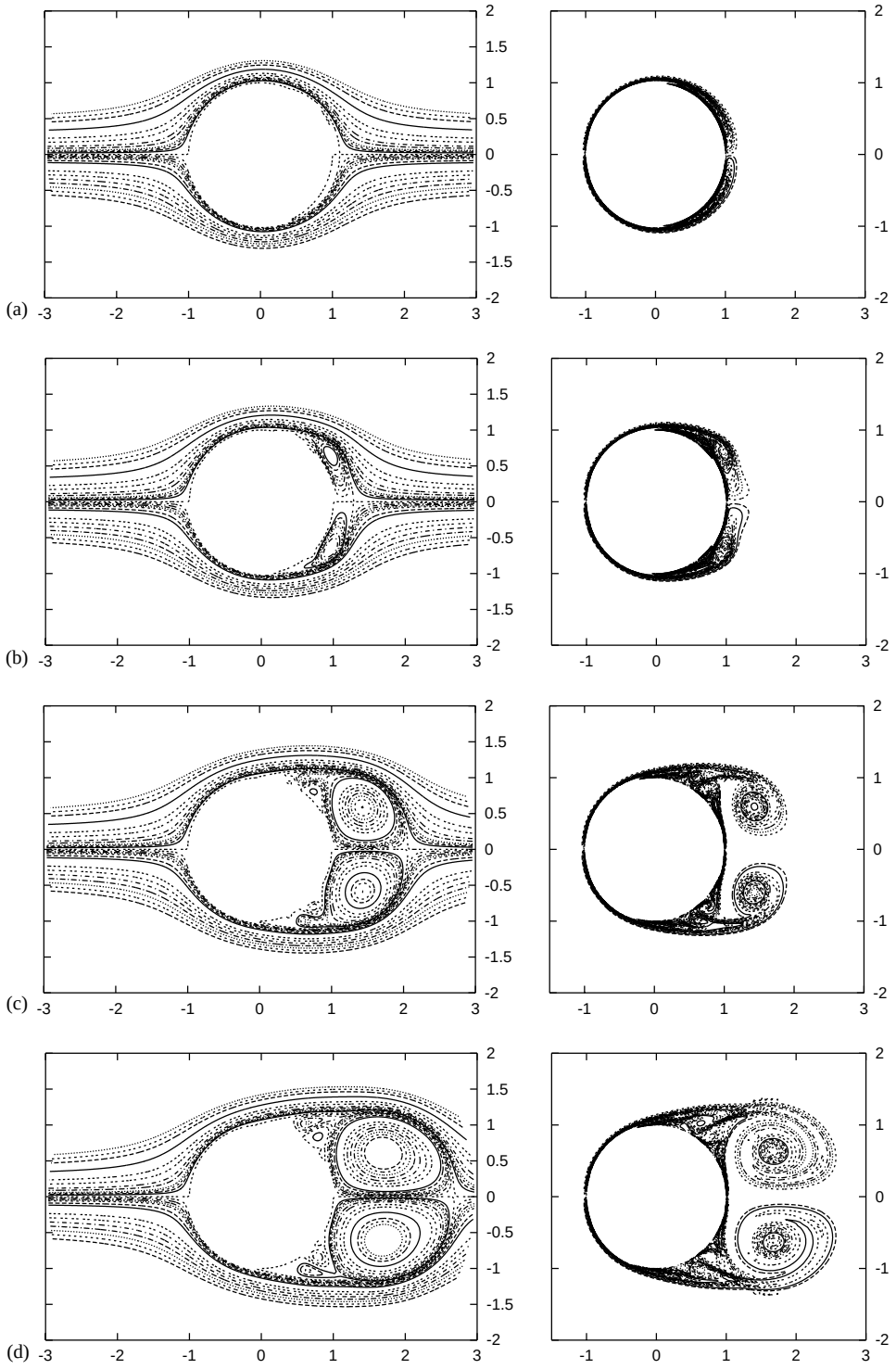

Fig. 4. Instantaneous streamfunction and vorticity contours at different reduced times, for the impulsively started cylinder and Re = 3000: (a) $tU/R = 1$; (b) $tU/R = 2$; (c) $tU/R = 4$; (d) $tU/R = 6$. The computations are performed for a domain with $R_\Gamma = 50$, $NX = 200$, $NY = 160$, and $\Delta t = 0.005$.

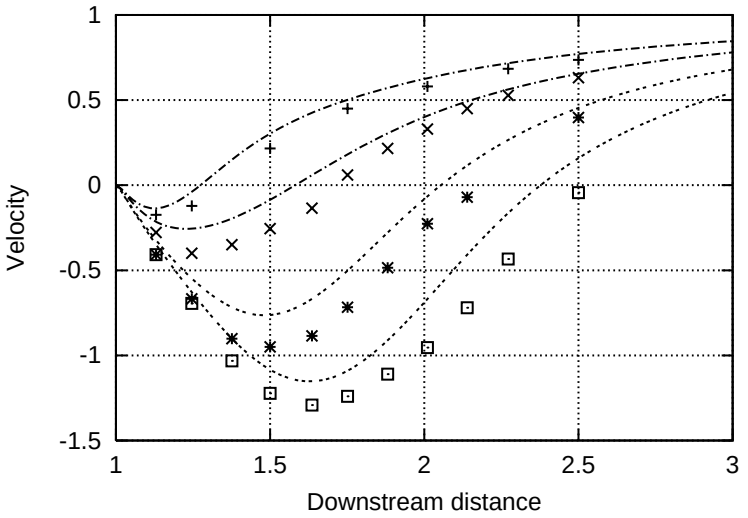

Fig. 5. Instantaneous profiles of the streamwise velocity along the axis in the near wake of an impulsively started cylinder at Re = 3000. Experimental results from Loc and Bouard (1985): (+) $tU/R = 2$; (×) $tU/R = 3$; (∗) $tU/R = 4$; (□) $tU/R = 6$; and present numerical results, using the lines, for $tU/R = 2-6$ from top to bottom. The computations are performed for a domain with $R_\Gamma = 50$, $NX = 200$, $NY = 160$, and $\Delta t = 0.005$.

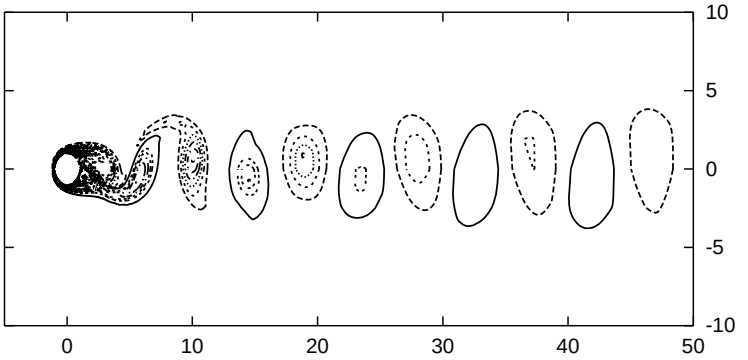

Fig. 6. Instantaneous vorticity contours in the wake of a circular cylinder at Re = 200. The computations are performed for a domain with $R_\Gamma = 50$, $NX = 200$, $NY = 160$. The time step $\Delta t = 0.01$.

$NX = 160$, $NY = 120$. As shown in the figure, there is good agreement between the present predictions and the results of Bard and Dennis (1985).

The initial stages of the motion are also examined for a cylinder with Re = 1000 and three velocity ratios, $V_r = 0.5$, 1, and 3. We use the same numerical parameters as in the previous example, except for $V_r = 3$ where the time step is reduced to $\Delta t = 0.005$. The unsteady evolution of the lift coefficient is shown in Fig. 9, which also reports some of the results from Bard et al. (1989). Except for the initial starting phase, the behavior of the unsteady lift at $V_r = 0.5$ and 1 is consistent with the corresponding results in Bard et al. (1989). For $V_r = 3$, differences with results in Bard et al. (1989) are more pronounced; however, a comparison of the vortex development near the cylinder and its interaction with the boundary layer in the results of Bard et al. (1989) shows that the computed flow fields exhibit the same features. Note that the present experiments show that the relative frame computations can deal with large variation of the angle of attack, since for $V_r = 1$ at $t = 24$ the cylinder has completed about six turns around its center.

Next, we verify the computed results for the stationary flow around the spinning cylinder in a uniform stream. To this end, we compare the computed results with those of Kang and Choi (1999), based on a cylinder with Reynolds number Re = 100 and three velocity ratios, $V_r = 0.5$, 1, and 1.5. The present computations are performed using a time step $\Delta t = 0.01$, and a domain with $R_\Gamma = 50$, $NX = 200$, and $NY = 160$. In Table 2 we compare our predictions of the

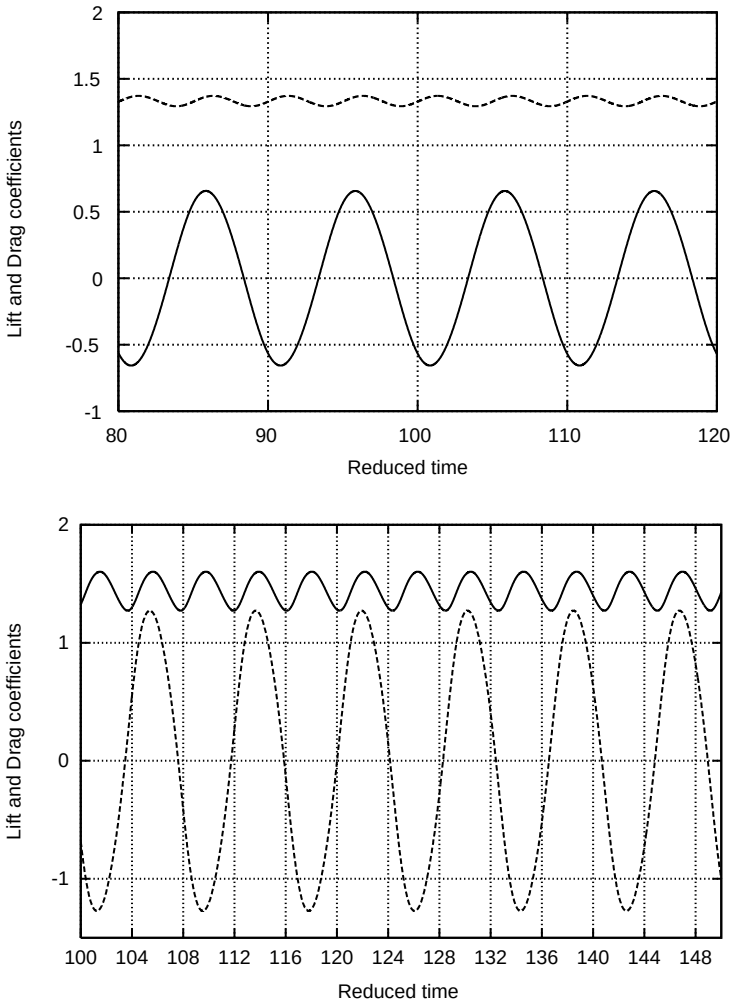

Fig. 7. Time evolution of the lift and drag coefficients for a stationary cylinder at Re = 200 (top) and Re = 855 (bottom): (———) C_L; (– – –) C_D. The computations are performed for a domain with $R_\Gamma = 50$, $NX = 200$, $NY = 160$. The time step $\Delta t = 0.01$.

Table 1
Fluid forces on a stationary cylinder at Re = 200 and 855

	Experimental		
	Re	C_D	St
	200	1.2	.19
	855	1.1	.21
	C_D	C_L	St
	Zang and Dalton (1997)		
Re = 200	1.25 ± 0.03	±0.54	0.196
Re = 855	1.2 ± 0.2	±0.95	0.238
	Lecointe and Picquet (1989)		
Re = 200	1.29 ± 0.04	±0.6	0.195
Re = 855	1.44 ± 0.23	±1.3	0.236
	Present		
Re = 200	1.33 ± 0.04	±0.65	0.201
Re = 855	1.43 ± 0.16	±1.27	0.235

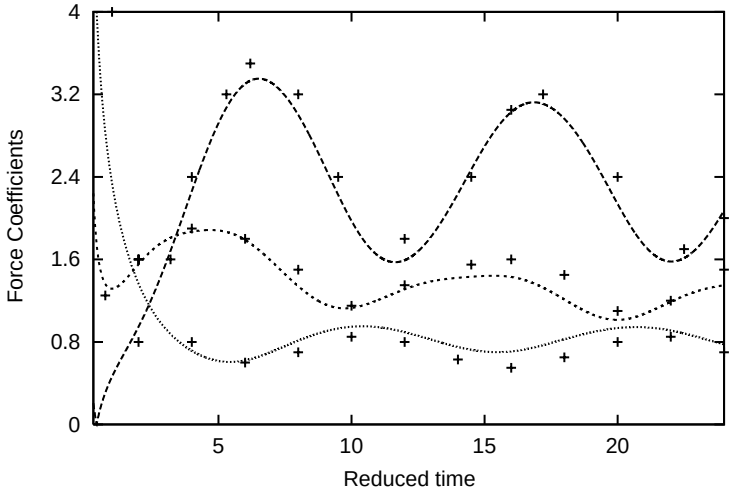

Fig. 8. Variation with reduced time (tU/R) of the lift (– – –), drag (- - - -), and torque (...) coefficients for the rotating cylinder with $V_r = 1$ and $\mathrm{Re} = 200$. Symbols (+) are used to denote the numerical results of Bard and Dennis (1985).

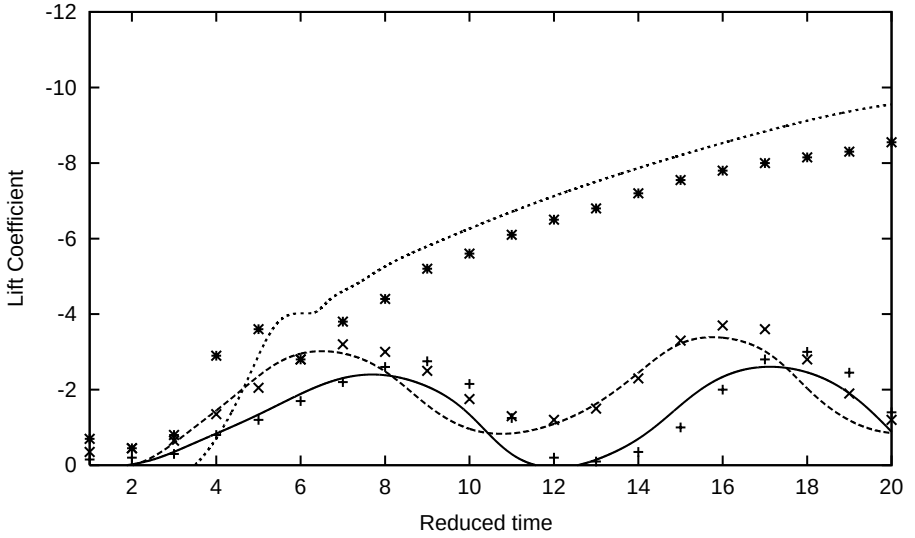

Fig. 9. Variation with reduced time (tU/R) of the lift coefficient for a rotating cylinder with $\mathrm{Re} = 1000$ and different V_r. Present computations: (——) $V_r = 0.5$; (– – –) $V_r = 1$; (- - -) $V_r = 3$; and symbols for the numerical results of Bard et al. (1989): (+) $V_r = 0.5$; ($\times$) $V_r = 1$; ($*$) $V_r = 3$.

Strouhal number (St), and the mean and fluctuation of the lift (C_L) and drag (C_D) coefficients with the results of Kang and Choi. Generally, a very good agreement is observed, though small but noticeable differences can be seen at $V_r = 1.5$. This completes the analysis of the rotating cylinder flow.

5.3. Oscillating NACA0012 Airfoil

Finally, to complete this section, the airfoil is now forced to rotate around a point located at the first third of the chord length. The angle of attack is given as a function of the normalized time t, according to

$$\alpha(t) = \alpha_0 - \tilde{\alpha}\cos(2\pi t), \tag{41}$$

Table 2
Fluid forces on a rotating cylinder at Re = 100 and $V_r = 0.5,\ 1$ and 1.5

	$V_r = 0.5$	$V_r = 1$	$V_r = 1.5$
	St		
Kang and Choi (1999)	0.187	0.186	0.183
Present	0.188	0.188	0.182
	C_L		
Kang and Choi (1999)	1.2 ± 0.52	2.15 ± 0.6	3.2 ± 0.58
Present	1.15 ± 0.57	2.28 ± 0.55	3.5 ± 0.52
	C_D		
Kang and Choi (1999)	1.3 ± 0.09	1.15 ± 0.16	0.85 ± 0.2
Present	1.3 ± 0.07	1.15 ± 0.14	0.97 ± 0.18

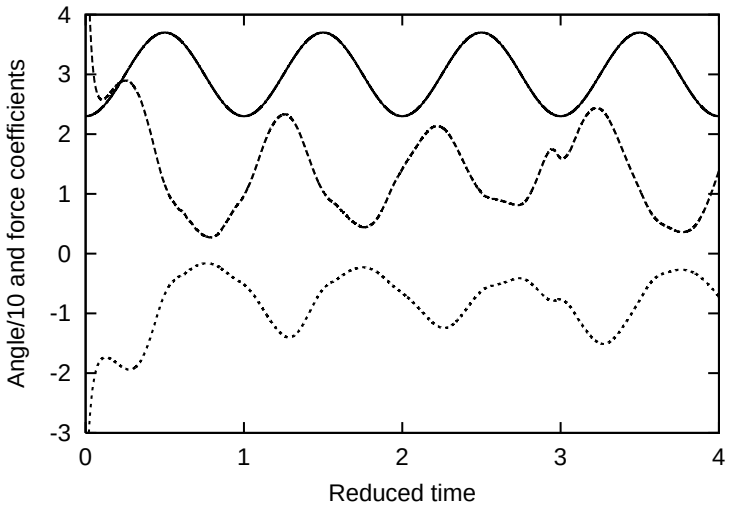

Fig. 10. Evolution with the reduced time (tU/L) of the lift (– – –), drag (- - - -) coefficients and angle of attack (——), for the oscillating airfoil. Amplitude of the oscillation is 7°. with a normalized period of 1. The mean angle of attack is 30°. and Re = 3000. Rotation center is located at the first third of the chord length. Numerical parameters are $NX = NY = 128$, $R_\Gamma = 35$, $\Delta t = 0.001$, seven grid levels.

where the time is normalized with the chord length, $\alpha_0 = 30°$ is the mean angle of attack and $\tilde{\alpha} = 7°$ the amplitude of the motion. The Reynolds number based on inflow velocity, viscosity, and chord length is 3000. The numerical parameters are $NX = NY = 128$, $R_\Gamma = 35$, $\Delta t = 0.001$ and eight grid levels are used. Since both the motion amplitude and mean value of the angle of attack are large, once again the flow does not remain attached, and large recirculation zones on the upper surface are reported. In Fig. 10 we have depicted the evolution of the lift and drag coefficients with time. Compared to the fixed airfoil case, the fact of driving the rotation causes the flow to respond mainly at the forced frequency (with a characteristic period of 1). The curves of Fig. 10 can be compared with the results of Ohmi et al. (1991) to show that the estimated fluid force characteristics are correctly computed. Note that our results contain less high-frequency fluctuations (i.e., are smoother) as compared to Ohmi et al. (1991).

6. Estimation of flutter derivatives

In this section, we recall some results of the flutter theory of a thin airfoil for a more extensive discussion of the theory, see Scanlan, 2000; Scanlan and Jones 1999. Next, we describe various experimental methodologies (e.g., Scanlan

and Tomko, 1971; Beith, 1998; Iwamoto and Fujino, 1995) that are presently used to estimate the flutter derivatives of a given (airfoil or bridge deck) section. The numerical experiments presented in the next sections closely follow these methodologies, and the basic ideas of the procedures are briefly outlined below.

6.1. Theory of flutter derivatives

The basic idea of the flutter derivatives lies in the identification of the motion-related fluid forces exerted on an airfoil, or, more particularly on a 2-D section of it. This process assumes a linear relation between force functions and the laws of motion of the airfoil so that superposition, or conversely decomposition, in both frequency and freedom spaces is allowed. Such a linear decomposition limits the validity of the approach to small-amplitude motions. For a streamlined airfoil undergoing smooth oscillations with a circular frequency ω in a uniform free stream of velocity V_∞, Scanlan and Tomko (1971) provide the following expansion:

$$L = \frac{\rho V_\infty^2}{2}(2b)\left[kH_1^*\frac{\dot{\tilde{h}}}{V_\infty} + kH_2^*\frac{b\dot{\alpha}}{V_\infty} + k^2H_3^*\alpha\right], \tag{42}$$

$$M = \frac{\rho V_\infty^2}{2}(2b^2)\left[hA_1^*\frac{\dot{\tilde{h}}}{V_\infty} + kA_2^*\frac{b\dot{\alpha}}{V_\infty} + k^2A_3^*\alpha\right], \tag{43}$$

where L and M are the aerodynamic lift and torque; ρ is the air density; $b = B/2$ is the airfoil half chord-length; kH_1^*, kH_2^*, $k^2H_3^*$, kA_1^*, kA_2^* and $k^2A_3^*$ are the flutter derivatives of the studied airfoil; and $k = b\omega/V_\infty$ is the reduced frequency of the motion. The flutter derivatives are functions of the reduced frequency k, and in practice we seek the aerodynamic coefficients H_1^*, H_2^*, H_3^*, A_1^*, A_2^*, and A_3^* appearing in Eqs. (42) and (43). These expressions clearly show the linear dependence of the fluid forces acting on the airfoil in relation to the accelerations and velocities of the two displacement variables h and α. $\dot{\tilde{h}}$ corresponds to the transverse velocity (relative to the free-stream velocity), measured at the airfoil mid-chord. The tilde is added in order to distinguish the velocity at mid-chord, which combines with $\dot{\alpha}$ whenever the rotation center is not located at the mid-chord point, from the solid-body "vertical" velocity of the airfoil: $\dot{h}$. In the following we restrict our attention to airfoils that are permitted to rotate around their mid-chord point. Hence $\dot{\tilde{h}} \equiv \dot{h}$, and we drop the tilde in the remaining part of the paper. The determination of the flutter derivatives is now discussed in the following subsections.

6.2. Extraction from forced-motion

By virtue of the linear expansion of the related-motion force functions equations (42) and (43), the flutter derivatives H_1^* and A_1^* associated to h-motion (resp. H_2^*, H_3^*, A_2^*, and A_3^* for α-motion) can be measured from forced-motion experiments at a fixed reduced frequency k. The experiment consists in measuring the lift and torque of an airfoil subject to pure vertical (or torsional) oscillations, and then to extract the in-phase and out-of-phase components corresponding to the reduced frequency k. For instance, let us consider the following time variation of the angle of attack:

$$\alpha(t) = \alpha_0 \sin \omega t, \tag{44}$$

then, according to Eqs. (42) and (43) we obtain

$$\frac{L(t)}{\alpha_0 k^2 \rho V^2 b} = \left[H_2^* \cos \omega t + H_3^* \sin \omega t\right], \tag{45}$$

$$\frac{M(t)}{\alpha_0 k^2 \rho V^2 b^2} = \left[A_2^* \cos \omega t + A_3^* \sin \omega t\right]. \tag{46}$$

Thus, H_3^* (A_3^*) can be computed from the component of the lift (torque) signal in phase with the oscillation, while H_2^* (A_2^*) can be obtained from the out-of-phase component of the lift (torque) signal. Applying the same analysis to pure vertical oscillations, we find that H_1^* and A_1^* can be deduced from the out-of-phase components of the corresponding lift and torque signals. The experiments must be repeated for each reduced frequency k of interest. The main difficulty of this approach is the extraction of the fluid loads from measurements which usually combine the fluid loads and the inertia forces due to the body motion. However, from the computational point of view, this does not pose a significant challenge since the fluid loads are computed independently from the flow solution. Moreover, since the motion of the airfoil is prescribed, the coupling between the flow and the airfoil dynamics is not considered in this kind of experiments. Numerical extraction of the flutter derivatives using the forced-motion approach is considered in Section 7.

6.3. Extraction using spring-mounted airfoil

Determination of the flutter derivatives can also be based on the analysis of the variations of the apparent damping ratios and natural mechanical frequencies of the airfoil when placed in the free stream. To describe the methodology, we consider a spring-mounted airfoil which is allowed to rotate around its mid-chord point. Accordingly, the dynamics of the airfoil are governed by the linear oscillator equation:

$$I\left(\ddot{\alpha} + 2\omega_\alpha \zeta_\alpha \dot{\alpha} + \omega_\alpha^2 \alpha\right) = M(t). \tag{47}$$

Introducing the expansion of Eq. (43) we can rewrite Eq. (47) as

$$\ddot{\alpha} + 2\zeta_{\alpha w}\omega_{\alpha w}\dot{\alpha} + \omega_{\alpha w}^2 \alpha = 0, \tag{48}$$

where

$$2\zeta_{\alpha w}\omega_{\alpha w} = 2\zeta_\alpha \omega_\alpha - \frac{\rho V_\infty}{I} b^3 (k A_2^*), \tag{49}$$

$$\omega_{\alpha w}^2 = \omega_\alpha^2 - \frac{\rho V_\infty^2}{I} b^2 (k^2 A_3^*). \tag{50}$$

Thus, $\zeta_{\alpha w}$ is the apparent damping ratio in torsion and $\omega_{\alpha w}$ is the apparent mechanical frequency for the system surrounded by the flow (the subscript w stands for "wetted"). It is clear that one may expect the experimental device to preserve the positiveness of the square of the apparent mechanical frequency (so its stiffness), namely $\omega_{\alpha w}^2 > 0$, to ensure that the system exhibits finite amplitude oscillations. This constraint is expressed using the following inequality:

$$\omega_{\alpha w}^2 > 0 \quad \Rightarrow \quad I\omega_\alpha^2 > \rho V_\infty^2 b^2 (k^2 A_3^*). \tag{51}$$

Assuming that the airfoil is well balanced, that is the latter criterion is satisfied, then the asymptotic motion has the following form:

$$\alpha_\infty(t) = \alpha_0 \exp^{\lambda_{\alpha w} t}, \tag{52}$$

where $\lambda_{\alpha w} = -d_{\alpha w} + \mathrm{i}\bar{\omega}_{\alpha w}$ is related to the apparent damping ratio and natural frequency through

$$d_{\alpha w} = \zeta_{\alpha w}\omega_{\alpha w}, \tag{53}$$

$$\bar{\omega}_{\alpha w}^2 = \omega_{\alpha w}^2\left(1 - \zeta_{\alpha w}^2\right) \approx \omega_{\alpha w}^2. \tag{54}$$

Therefore, the experiment consists in measuring the characteristics of the damped oscillation of the airfoil. Once $\zeta_{\alpha w}$ and $\omega_{\alpha w}$ are estimated, Eqs. (49)–(50) can be used to determine A_2^* and A_3^*. ζ_α and ω_α are measured from an experiment without inflow ($V_\infty = 0$). Similarly, when the characteristics of the asymptotic motion equation (52) are known from measurement, H_2^* and H_3^* are determined from the component of the lift in phase with $\dot{\alpha}_\infty$ and with α_∞. The same analysis applies for an airfoil undergoing vertical motion only, with the remaining coefficients H_1^* and A_1^* as results.

7. Forced motions

The numerical experiments below follow the same approach described in Section 6.2. Starting from the steady flow, the airfoil is subjected to prescribed oscillations and the computations are carried for four periods in order to go beyond the initial transient. Then the resulting fluid forces recorded on the last period are projected in Fourier space to extract the corresponding flutter derivatives. The experiment is repeated for the two motions (pure translation and rotation) and each frequency. Flutter derivatives are given as functions of the reduced velocity V_∞/Nb (Scanlan and Tomko, 1971), where $k/2\pi$.

7.1. NACA0012 Airfoil

We start by computing the flutter derivatives for an NACA0012 airfoil. To this end, forced-motion simulations are conducted using the following driving signals:

$$h(t) = 0.05b \sin \omega t, \quad \alpha(t) = 2\sin \omega t \quad (deg).$$

The computed values of the flutter derivatives are plotted in Fig. 11, which also reports theoretical results for a zero-thickness airfoil (flat plate) in an inviscid flow. These theoretical values are commonly used in preliminary aircraft design, but are the solution of a problem that is not fully equivalent to the one solved in the present work. Thus, full

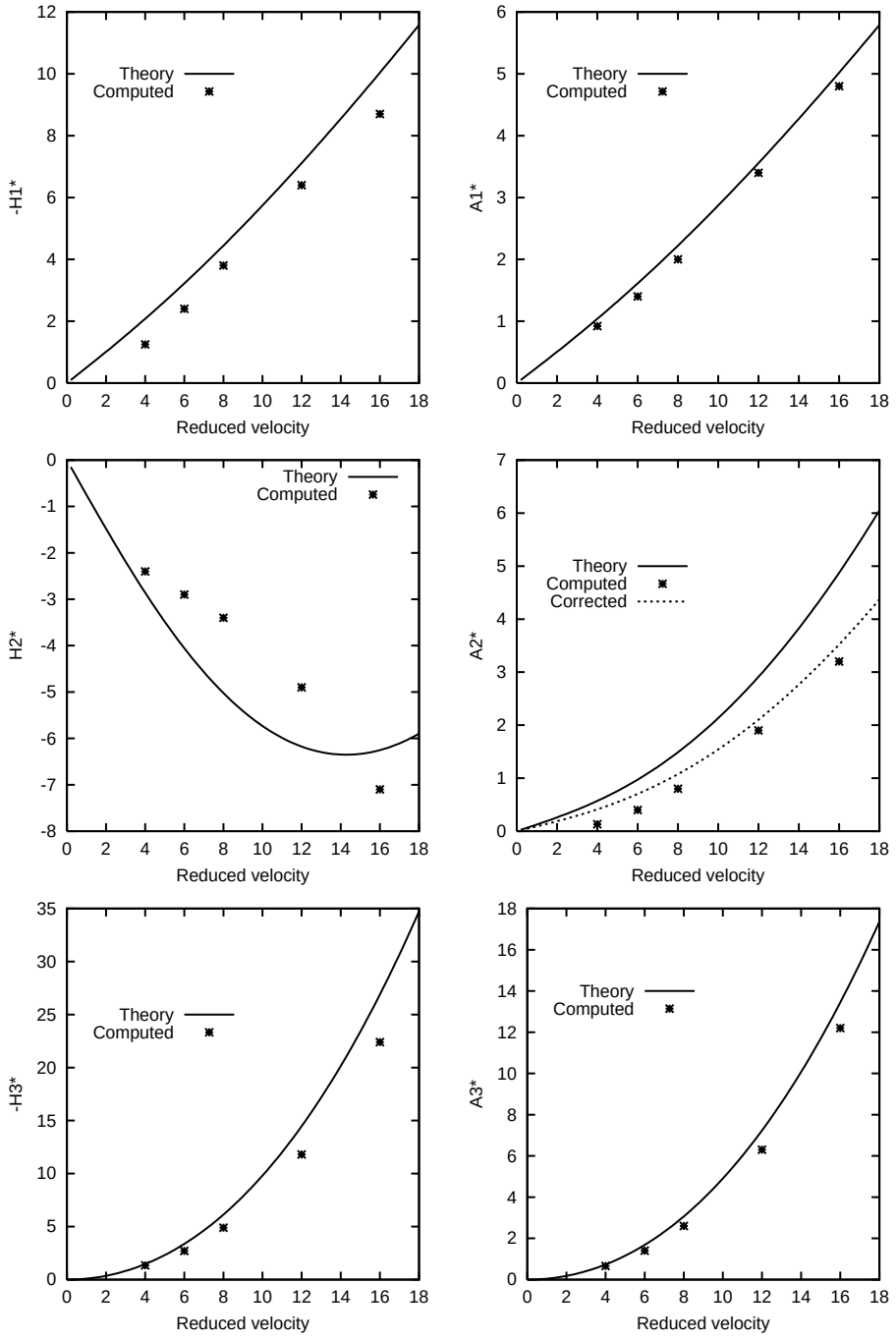

Fig. 11. Computed flutter derivatives ($*$) of an NACA0012 airfoil as a function of the reduced velocity V/Nb. Theoretical values (solid lines) are also shown for comparison. The results are obtained using forced-motion simulations. The computations are performed on a domain with $R_\Gamma = 25$, using a grid with 128×128 grid points. The Reynolds number based on chord length $\mathrm{Re} = 800$, and the time step $\Delta t = 0.01$.

agreement between the theoretical and computational results is not expected, but the comparison still provides us with valuable insight.

It can be observed that the computed values of H_1^* and A_1^* are close to the theoretical results, but that the computations lead to slightly lower predictions. Lower computed values are also reported for A_2^* (effect of $\dot{\alpha}$ on the

torque), but with larger and increasing differences when the reduced velocity is increased. Large differences have also been reported in the physical experiments of Scanlan and Tomko (1971), who proposed to correct the theoretical values by a factor of $4.54/2\pi$ in order to account for the geometrical differences between the NACA0012 airfoil and the flat plate. The corrected theoretical results for A_2^* are also reported in Fig. 11. With this correction we get a much better agreement between the present computations and the theory.

For H_2^* (effect of angular velocity on the lift), the agreement between theoretical and computed values is poor and trends are also different. In particular, the theory predicts that H_2^* has a minimum at $V/Nb \approx 14$. This trend is not observed in the computations. A similar disagreement was also reported in physical measurements given by Scanlan and Tomko (1971).

Finally, Fig. 11 shows that the computed values of A_3^* and H_3^* are in good agreement with the theoretical results, and that both the computed and theoretical predictions reveal the same trends. One can still note small differences in the magnitude of the coefficients that increase with increasing reduced velocity. Again the computations provide lower values for H_3^* and A_3^* than the theory predicts. Thus, except for H_2^*, the computed predictions are consistent with the corresponding theoretical results.

As noted earlier, close complete agreement between theory and computations is not to be expected, in particular due to finite thickness and Reynolds number effects. Additional computations are performed below in order to examine these effects.

7.2. Ellipses

In this section the effect of the section thickness is investigated based on forced-motion experiments for different ellipses. The thickness ratio, denoted T_r, is defined as the ratio of the ellipse thickness to the chord length. We consider four thickness ratios, $T_r = 0.21$, 0.142, 0.08, and 0.026, and perform simulations using the same Reynolds number and numerical parameters as in the previous set of computations. Results are reported in Fig. 12 which depicts the dependence of the computed flutter derivatives on the reduced velocity V_∞/Nb.

The results show that the relative thickness of the ellipse has a noticeable influence on the lift-related coefficients, H_1^*, H_2^*, and H_3^*. Specifically, the magnitude of these coefficients increases with a decreasing thickness ratio. This trend could explain why the computed values of H_1^* and H_3^* for the airfoil are smaller than the theoretical values of the flat plate. In addition, the results suggest that the finite thickness of the sections considered in this work does not seem to be responsible of the large deviation of H_2^* from the inviscid theory, since this deviation increases as the thickness ratio decreases.

Further examination of the curves given in Fig. 12 shows that the torque-related coefficients are much less affected by the relative thickness. In fact, except for the highest value of T_r considered in the study, the torque coefficients A_1^* and A_3^* are nearly unaffected by Tr, especially at the lower values of the reduced velocity. For A_2^*, at the lowest values of Tr, we observe an attenuation of the computed magnitude as the reduced velocity is increased. Here, an under-resolution of the computational grid could be responsible for this trend.

Based on the results of the present experiments, one may conclude that: (i) the section thickness mainly affects the coefficients related to transverse motion, (ii) the magnitudes of the H_1^*, H_2^*, and H_3^* increase as the thickness ratio decreases, (iii) the discrepancy between the computed values of H_2^* and the theoretical flat-plate prediction does not appear to be due to a finite-thickness effect; and (iv) torsion-related coefficients are not very sensitive to the section thickness, as long as the thickness ratio is small.

7.3. Reynolds effects

As discussed earlier, the present approach is based on selecting moderate values of the Reynolds number, which enables us to perform well-resolved direct simulations of the flow. The choice of Re is somewhat arbitrary but is generally orders of magnitude smaller below values characteristic of real applications. Consequently, for the approach to be useful, the predictions should exhibit weak dependence on the Reynolds number. We briefly address this issue by performing additional simulations with different values of Re. We focus once again on the NACA0012 airfoil considered in Section 7.1, and obtain flutter derivative predictions for $\mathrm{Re} = 600$ and 1200. The same domain size is used but the spatial discretization and time step are varied in order to ensure adequate resolution of viscous boundary layer as well as stability of the computations.

Computed values of the flutter derivatives are plotted in Fig. 13. It can be seen in this figure that H_1^* and H_3^* coefficients are not strongly affected by the value of the Reynolds number, in contrast to H_2^* which exhibits significant dependence on Re, especially for reduced velocities $V_\infty/Nb > 8$. The same trend is observed for the torque-related coefficients. Specifically, A_1^* and A_3^* are practically unaffected by the value of Re. Meanwhile, the estimates for A_2^* are

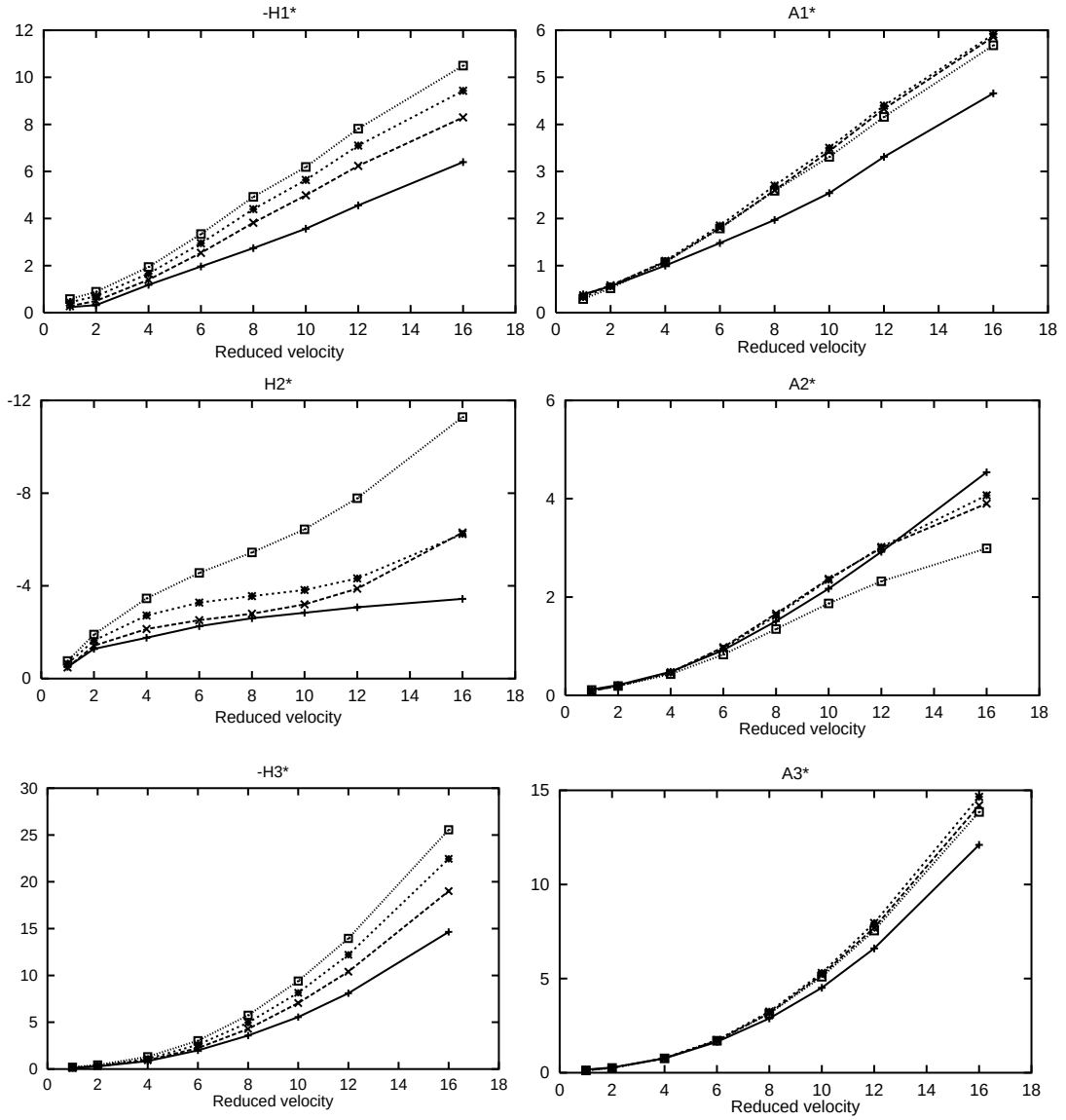

Fig. 12. Computed flutter derivatives as a function of the reduced velocity V/Nb for ellipses with different thickness ratios: (□) $T_r = 0.026$; (∗) $T_r = 0.080$; (×) $T_r = 0.142$; (+) $T_r = 0.210$. Numerical parameters as in Fig. 11.

essentially independent of Re in the range $V_\infty/Nb < 8$, but exhibit a noticeable variation with Re at higher values of the reduced velocity. Thus, one can conclude that the computed coefficients related to the rotational velocity $\dot{\alpha}$ are affected by the choice of the Reynolds number when large reduced velocities are considered. Using the present computational approach, it appears difficult to obtain sharp, Re-independent estimates of H_2^* and A_2^* from the forced-motion simulations.

7.4. Influence of amplitude of motion

We conclude our discussion of forced-motion approach by analyzing the effect of the amplitude of the imposed forcing signals. To this end, we focus on the NACA0012 airfoil and systematically vary the amplitudes of the transverse and torsional motions. The Reynolds number, grid resolution, and time step are the numerical parameters which are the

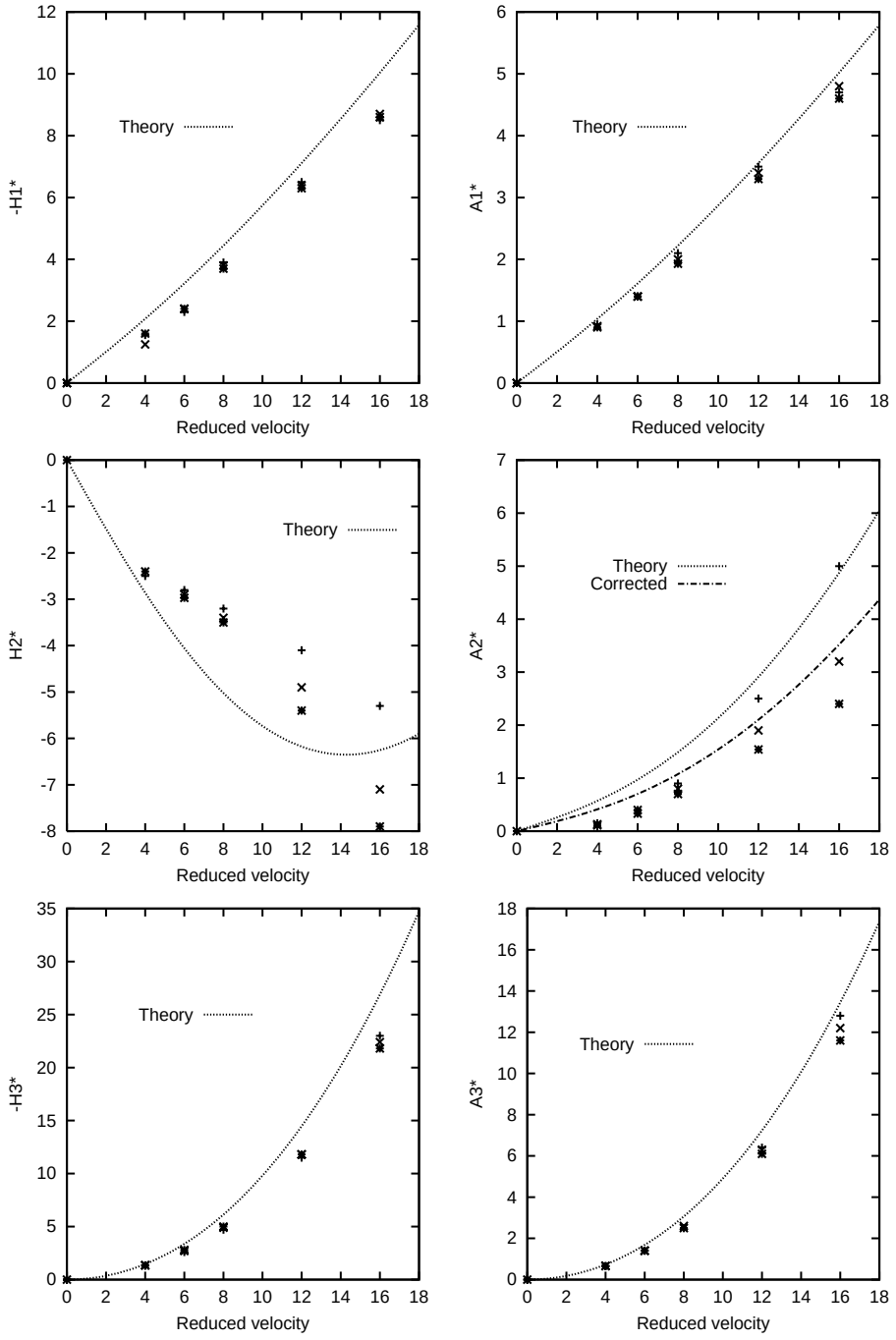

Fig. 13. Effect of the Reynolds number on the computed flutter derivatives of an NACA0012 airfoil. The results are obtained using forced-motion simulations with: Re = 600 (∗); Re = 800 (×); Re = 1200 (+). Theoretical (inviscid) values are also reported using solid lines. The computational grid has 128×128 grid points. A time step of 0.01 is used for Re = 600 and 800, while $\Delta t = 0.005$ for Re = 1200.

same as in Section 7.1, but the domain size is extended to $R_\Gamma = 30$. The reduced velocity is fixed at $V_\infty/Nb = 8$ and the flutter derivatives are computed for different forcing amplitudes.

Recalling that H_1^* and A_1^* are related to cross-stream motion, we compute them using reduced displacements (relative to that of b) equal to 0.02, 0.05, 0.10, 0.15, and 0.20. The results are given in Figure 14. The curves show that in the

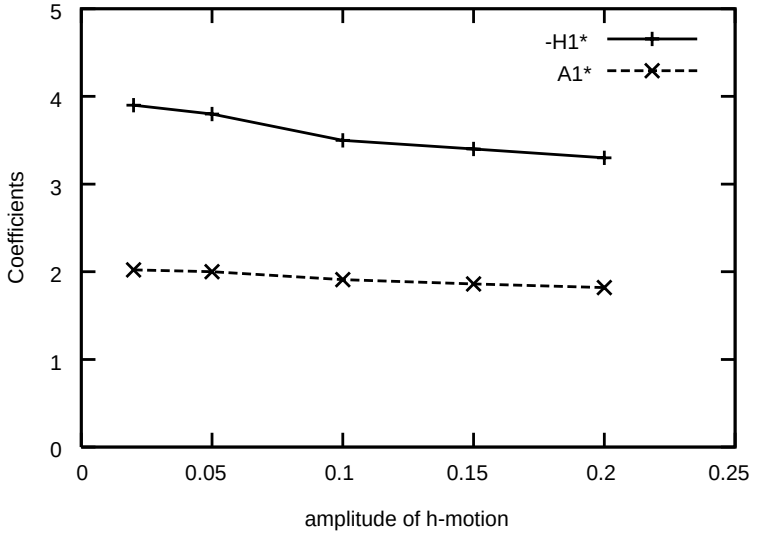

Fig. 14. Effect of the transverse motion amplitude on H_1^* (+) and A_1^* (×). The reduced velocity $V_\infty/Nb = 8$. Numerical parameters as in Fig. 11.

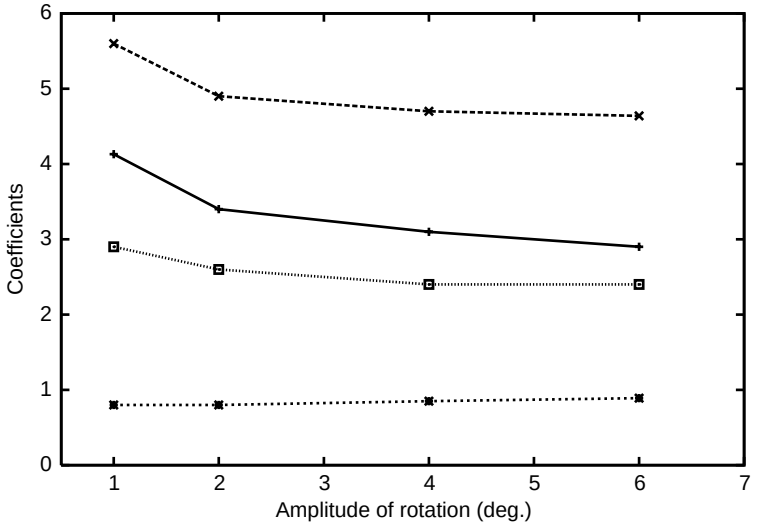

Fig. 15. Effect of torsional motion amplitude on $H_2^*(+), H_3^*(\times)$, A_2^* (∗), and A_3^* (□). The reduced velocity $V_\infty/Nb = 8$. Numerical parameters as in Fig. 11.

range considered A_1^* is practically unaffected by the amplitude of the transverse motion. In contrast, the computed values of H_1^* exhibit an appreciable dependence on the transverse displacement amplitude. In particular, H_1^* tends to decrease as the amplitude of the oscillations increases. In addition, H_1^* does not appear to exhibit a simple dependence on the motion amplitude, and so that extrapolation to infinitesimal amplitude is not straightforward. This behavior may also contribute to the aforementioned disagreement between computed and theoretical estimates of H_1^*.

The effect of the amplitude of the torsional motion is analyzed in a similar fashion. Specifically, simulations are performed at fixed reduced velocity, $V_\infty/Nb = 8$, using the following forcing amplitudes: 1°, 2°, 4°, and 6°. (Note that even for the largest amplitude tested (6°), for $V_\infty/Nb = 8$ the flow remains attached on the airfoil surface so that the linear expansion given in Eqs. (42) and (43) remains valid.) Computed flutter derivatives are plotted in Fig. 15. The results show that, except for the lowest amplitude tested (1°), the computed coefficients are not significantly affected when the angular motion amplitude of the motion is increased. In fact, it appears that as the amplitude is reduced, the

relative error on the computed fluid loads increases so that the extraction of the coefficients becomes inaccurate. Further tests (not shown) indicate that for angular motion amplitudes smaller than 1°, it is difficult to obtain consistent estimates of the motion coefficients.

8. Spring-mounted airfoil

In this section we apply the methodology described in Section 6.3 for the numerical prediction of the flutter derivatives of an NACA0012 airfoil. This methodology requires simulation of the spring-mounted airfoil problem and use of the numerical solution to determine the effect on the free stream on the airfoil oscillations.

8.1. Parameters and normalization

Instead of using dimensional quantities in Eqn (23) it has been found more convenient to treat the problem in its dimensionless form. We select b as characteristic length scale, V_∞ as characteristic velocity and $\rho V_\infty^2/2$ as the characteristic pressure. The characteristic time is then b/V_∞ and the normalization of the equations yields the dimensionless mass and mass moment of inertia ($\bar{M}$ and $\bar{I}$), reduced mechanical damping ratios for the transverse and torsional motions ($\bar{\zeta}_h$ and $\bar{\zeta}_\alpha$) and reduced natural mechanical frequencies ($\bar{f}_h$ and $\bar{f}_\alpha$), and the aspect ratio $H = h/b$.

In the computations below, the reduced mechanical damping ratios of the airfoil are fixed; we use $\bar{\zeta}_h = \bar{\zeta}_\alpha = 1/100$. Meanwhile, the values of $\bar{M}$, $\bar{I}$, $\bar{f}_h$, and $\bar{f}_\alpha$ are selected to obtain the desired response of the system. In practice, $\bar{f}_h$ and $\bar{f}_h$ are chosen so that the airfoil undergoes oscillations at the reduced velocity of interest, and $\bar{M}$ and $\bar{I}$ are tuned so that the fluid loads are more (when they are decreased) or less (when they are increased) felt by the airfoil. Note that in the limits $\bar{\zeta}_h, \bar{\zeta}_\alpha \to 0$ and $\bar{M}, \bar{I} \to \infty$ one would recover the forced-motion case. Also, using the present conventions the simulation conditions are described by $\bar{M}$, $\bar{\zeta}_h$, $\bar{f}_h$, and Re for transverse motion analysis, and by $\bar{I}$, $\bar{\zeta}_\alpha$, $\bar{f}_\alpha$, and Re for torsional motion.

8.2. Example of numerical results

Fig. 16 depicts typical results of a simulation of an airfoil undergoing free-oscillations around its half-chord point. In this example, Re = 800, $\bar{\zeta}_\alpha = 1/100$, $\bar{I} = 30$, and $\bar{f}_\alpha = 0.07$. The numerical experiment starts from a flow at rest. Then the Navier–Stokes equations are integrated over a period of five dimensionless time units. During this first stage, the

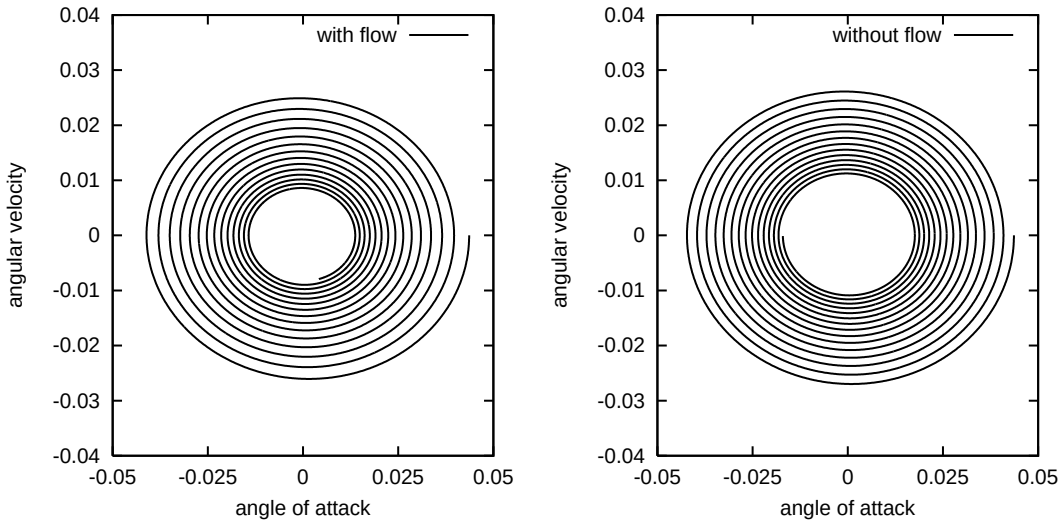

Fig. 16. Typical response for spring-mounted airfoil undergoing oscillations around its half-chord point. Plotted on the left is the rotation velocity against the angle of attack. The Reynolds number is 800, $\bar{I} = 100$, $\bar{f}_\alpha = 0.1$, and $\bar{\zeta}_\alpha = 1/100$. Other numerical parameters are the same as for Fig. 11. The effect of the free stream—which increases the damping rate—is illustrated by contrast with the right plot, which shows the response of the mechanical system alone.

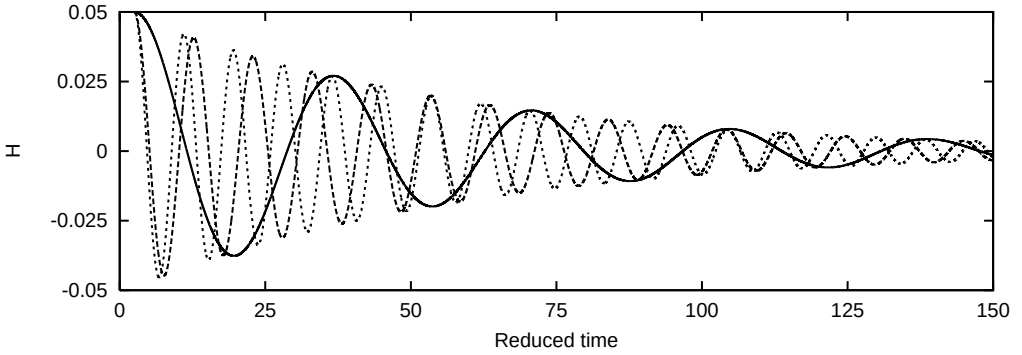

Fig. 17. Normalized displacement, H, versus reduced time, T, for three different natural frequencies of the mechanical system. The reduced damping $\bar{\zeta}_h = 1/100$, mass $\bar{M} = 100$. Numerical parameters as in Fig. 11.

airfoil remains fixed at its initial angle of attack. Following this initial stage, the airfoil is released, and damped-oscillation regime is consequently triggered. For analysis of torsional oscillations, an initial angle of attack of 2.5° is used.

The effect of the free stream on the airfoil dynamics is illustrated in Fig. 16 by contrasting the numerical solution (left) to a prediction that ignores the aerodynamics loads (right). Clearly, the presence of aerodynamic loads leads to a more rapid contraction of the system trajectory. Note that using a lighter airfoil (i.e., decreasing $\bar{I}$), and keeping $\bar{f}_\alpha$ constant, would lead to an even faster contraction of the system trajectory. This trend persists until $\bar{I}$ becomes too small to ensure the stability of the system.

Results for the transverse motion are shown in Fig. 17, which depicts the evolution of the displacement signals for different reduced frequencies. The results are obtained using $\bar{M} = 100$, $\bar{\zeta}_h = 2\pi/100$, and $\mathrm{Re} = 800$. In these simulations, the angle of attack α is set to zero and the initial transverse displacement $H = 0.05$. As in the analysis of torsional motion, the simulations start from rest and the flow first develops during five dimensionless time units of time before the airfoil is allowed to move in the cross-stream direction. Following its release, the airfoil starts to oscillate and the amplitude of the oscillations decays exponentially, as shown in Fig. 17. It can be seen that the overall exponential decay is nearly the same for all the frequencies considered. This similarity is due to the nearly linear dependence of H_1^* on the reduced velocity, and the use of a constant mass $\bar{M}$.

8.3. Flutter derivatives

As was discussed earlier, the extraction of flutter derivatives is based on analyzing the differences between the exponential decay of the motions with and without free stream. The methodology is valid during the asymptotic stages of the decay, where the motion can be expressed in the form given in equation (52). Note, however, that the flow, and consequently the aerodynamic loads as well as the motion of the airfoil, exhibit a transient behavior after release of the airfoil. Therefore, the analysis is not necessarily valid during this transient. In the computations, the decaying oscillations and fluid load signals were recorded during the entire period following release, and the entire data set is processed. Not surprisingly, the computed damping rates and frequencies exhibit a scatter during the initial transient. We eliminate this scatter by dropping estimates obtained during the initial transient, and only report values obtained at larger times.

Fig. 18 shows the computed flutter derivatives for the NACA0012 airfoil. The theoretical values based on the inviscid, flat-plate analysis are also provided for comparison. As in the forced-motion experiments, there is good agreement between theory and computed values as for the coefficients related to $\dot{h}$ and α (i.e., H_1^*, A_3^*, H_3^*, and A_3^*). In addition, consistent with earlier observations, a noticeable discrepancy can be observed between the computed values of H_2^* and A_2^* and the corresponding theoretical predictions.

One can also note that the analysis yields sharp estimates of H_1^* and A_1^* and that in contrast the computed values of H_3^* and A_3^* exhibit an increasing scatter as the reduced velocity increases. Following the remarks in Section 7.4, this phenomenon may be due to the dependence of these coefficients on the amplitude of the motion, which in the present simulations is evolving with time. The results also reveal a large scatter in the computed values of H_2^* and A_2^* and, similar to experiences with the forced-motion approach, significant differences exist between the computed predictions and the theoretical results.

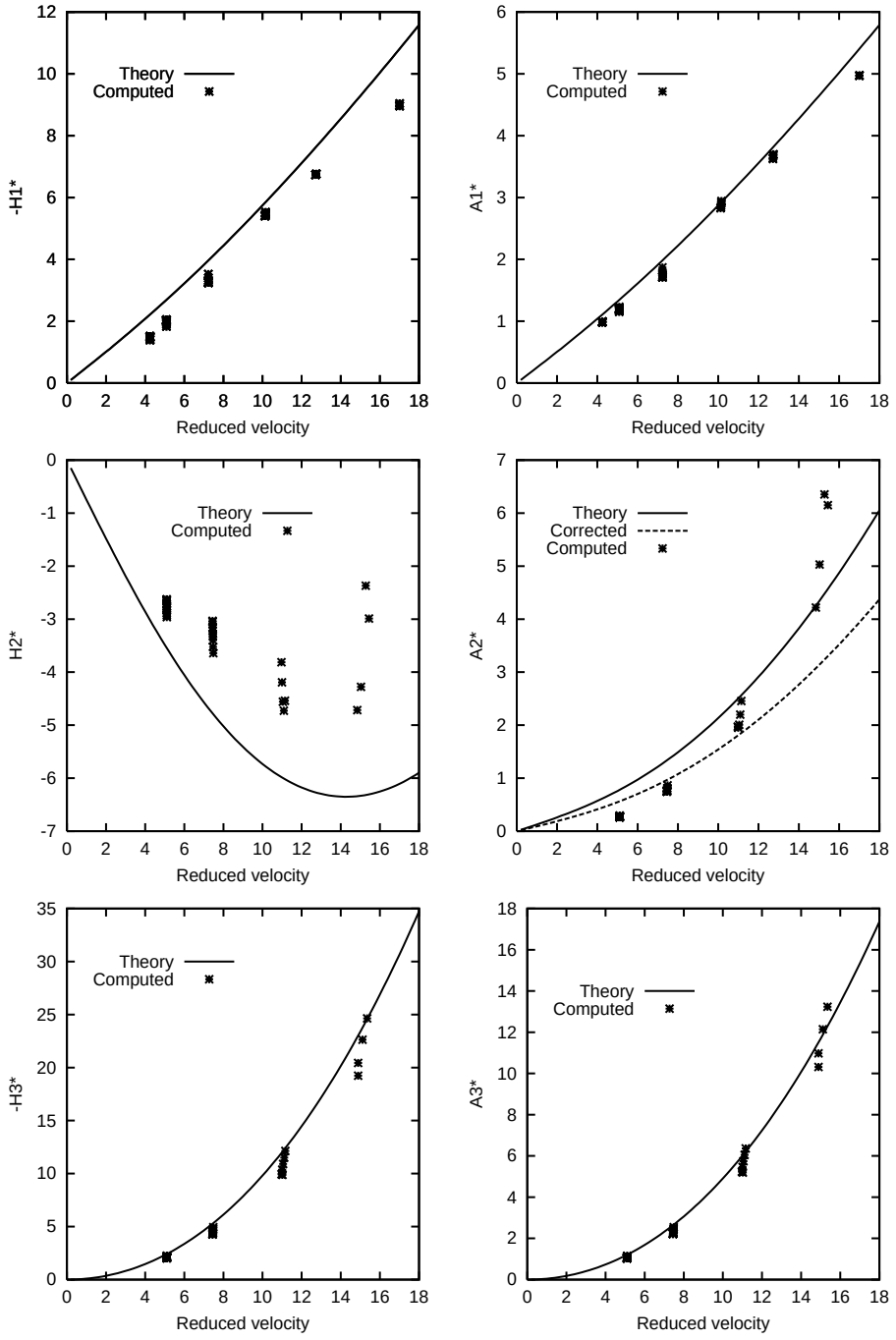

Fig. 18. Computed flutter derivatives ($*$) of the NACA0012 airfoil using the spring-mounted experiment. Theoretical results are also presented using the solid lines. Numerical parameters as in Fig. 11.

For $V_\infty/Nb > 10$, the results of the spring-mounted simulations are in good agreement with those of the forced-motion computations (11). For higher values, differences between the predictions of the two approaches can be observed. These differences are not surprising since, as shown by Scanlan and Tomko (1971), the computed flutter derivatives are not independent of the rate of the exponential decay. Thus it appears that there exists a compromise in

the numerical extraction of flutter derivatives. On the one hand, it is convenient to set the parameters of the experiment so that the deviation between the motion decay characteristics with and without free stream is large, i.e., the flow has a large impact on the airfoil response, which ensures accurate computation of the coefficients. On the other hand, a large influence of the flow on the motion decay means a large damping of the oscillations, so that the spectrum of the motion becomes broader, and identification of the fluid loads with a reduced velocity becomes less certain. This has significant implication for computational investigation of flutter coefficients at large reduced velocities. In these situations, only a few periods can be simulated within a moderate CPU time and, in order to obtain accurate estimates, it is essential that one observes significant variation of the amplitude of motion during "relatively short" simulation times.

9. Conclusion

The numerical estimation of the flutter derivatives of an NACA0012 airfoil requires the use of a computer code that solves the unsteady incompressible Navier–Stokes equations. In this work, we have derived a formulation based on the streamfunction/vorticity representation of the governing equations written in a relative frame attached to the airfoil. This approach allows us to consider arbitrary unsteady motions of the airfoil. The computer code has been successfully tested on various cases from the literature. Comparison has been made with both experimental and numerical earlier works. In most of the cases a good agreement has been obtained, providing confidence in the reliability of the method. These tests have covered problems involving impulsive and steady state responses, with fixed and moving boundary situations.

The simulation scheme is then applied to compute the flutter derivatives of an NACA0012 airfoil. Two approaches for the determination of motion coefficients are tested; these are based on: (a) analysis of the unsteady pressure loads on the airfoil undergoing forced oscillations and (b) an analysis of decaying oscillations of a spring-mounted airfoil. There is very good agreement between the computed predictions for reduced velocities smaller than 10, but differences are observed at higher values. A dependence of the computed coefficients on the imposed motion amplitude or the decay rate appears to be at the origin of the differences observed at high reduced velocities.

The computed predictions are compared with theoretical results for a flat plate in the inviscid limit. Very good agreement is observed for the coefficients related to the transverse motion (H_1^* and A_1^*) and to the angle of attack (H_3^* and A_3^*). On the other hand, significant differences are noted for coefficients related to the rotational velocity, H_2^* and A_2^*. For these coefficients, disagreement between measured and theoretical values has also been noted by Scanlan and Tomko (1971).

The simulations have also been applied to examine the effects of Reynolds number and profile thickness on the predicted flutter derivatives. Computed results indicate that torsion-related coefficients are not very sensitive to the section thickness, as long as the thickness ratio is small. However, the magnitudes of the coefficients related to transverse motion increase as the thickness ratio increases. The analysis also indicates that the computed values of A_1^*, A_3^*, H_1^*, and H_3^* are not strongly affected by Re. In contrast, the coefficients related to the rotational velocity $\dot{\alpha}$, A_2^* and H_2^*, are significantly affected by the value of the Reynolds number, especially when large reduced velocities are considered.

The present experiences indicate that, while the forced-motion and spring-mounted approaches yield consistent estimates, the former approach appears to be computationally more convenient for several reasons. These include the following. (i) The spring-mounted experiment requires a solution of a coupled fluid–structure interaction problem and thus involves a secondary solver for the airfoil dynamics. This introduces an additional error source and increases code complexity. (ii) Using the spring-mounted experiment, one is not able to determine, a priori, the frequency of the oscillation that the airfoil will exhibit. Consequently, successive approximations are necessary if the flutter derivatives are to be computed for a specific reduced velocity. In contrast, for the forced-motion approach, the frequency of the oscillations is prescribed. (iii) The forced-motion analysis seems to be more suited for the numerical investigation of flutter derivatives at large reduced velocities. This is due to the fact that the forced-motion approach requires only the simulation of a few periods of the motion. For short-duration simulations, the spring-mounted method requires a large decay rate, which may reduce the accuracy of the corresponding estimates; alternatively, the simulations can be extended over a large number of periods, which necessitates a higher CPU cost.

In addition, by exploiting linearity and superposition principles, it appears possible that flutter derivatives in a wide reduced-velocity range can be determined within a single forced-motion simulation. For instance, the full frequency range can be treated in the same experiment using a step (or Heaviside) law for the motion. The corresponding

approach, known as the indicial approach, has already been exploited by Brar et al. (1996). Their experiences suggest performing indicial calculations for step changes in $\dot{h}$ and $\dot{\alpha}$, by simulating linear ramps in the h and α displacements. The numerical method presented here naturally accommodates such computations, which will be addressed in future work.

Acknowledgements

O.L.M. wishes to acknowledge O. Daube for his useful comments and advice on the influence matrix technique, and the Johns Hopkins University for its financial support during visits of summer 2000. Acknowledgement is also made of the support of the U.S. National Science Foundation under Grant CMS 9705648 to the Johns Hopkins University.

References

Bard, H.M., Dennis, S.C.R., 1985. Time-dependent viscous flow past an impulsively started rotating and translating circular cylinder. Journal of Fluid Mechanics 158, 447–488.

Bard, H.M., Dennis, S.C.R., Young, P.J.S., 1989. Steady and unsteady flow past a rotating circular cylinder at low Reynolds numbers. Computers and Fluids 17, 579–609.

Bisplighoff, R.L., Ashley, H., 1962. Principles of Aeroelasticity. Dover, New York.

Beith, J.G., 1998. A practical engineering method for the flutter analysis of long span bridges. Journal of Wind Engineering and Industrial Aerodynamics 77–78, 357–366.

Brar, P.S., Raul, R., Scanlan, R.H., 1996. Numerical calculation of flutter derivatives via indicial functions. Journal of Fluids and Structures 10, 337–351.

Buzbee, B., Golub, G., Nilson, C., 1970. On direct method for solving poisson's equation. SIAM Journal of Numerical Analysis 7, 627–656.

Chang, C.-C., Chern, R.-L., 1991. A numerical study of the flow around an impulsively started circular cylinder by a deterministic vortex method. Journal of Fluid Mechanics 233, 243–263.

Daube, O., 1992. Resolution of the 2D Navier–Stokes equations in velocity–vorticity form by means of an influence matrix technique. Journal of Computational Physics 103, 402–414.

Deniz, S., Staubli, T., 1998. Oscillating rectangular and octagonal profiles : modeling of fluid forces. Journal of Fluids and Structures 12, 859–882.

Fletcher, C.A.J., 1988. . Computational Techniques for Fuid Dynamics, Vol. I. Springer, New-York.

Iwamoto, M., Fujino, Y., 1995. Identification of flutter derivatives of bridge deck from free vibration data. Journal of Wind Engineering and Industrial Aerodynamics 54–55, 55–63.

Kang, S., Choi, H., 1999. Laminar flow past a rotating circular cylinder. Physics of Fluids 11, 3312–3321.

Larsen, A., Walther, J.H., 1998. Discrete vortex simulation of flow around five generic bridge deck sections. Journal of Wind Engineering and Industrial Aerodynamics 67–68, 239–252.

Lecointe, Y., Picquet, J., 1989. Flow structure in the wake of an oscillating cylinder. ASME Journal of Fluids Engineering 111, 139–148.

Loc, T.P., Bouard, R., 1985. Numerical solution of the early stage of the unsteady viscous flow around a circular cylinder: a comparison with experimental visualization and measurements. Journal of Fluid Mechanics 160, 93–117.

Mc Cormick, S.F., 1987. Multigrids Methods, Vol. 3. SIAM Books, Philadelphia.

Milne-Thomson, L.M., 1968. Theoretical Hydrodynamics, 5th Edition. Dover, New York.

Ohmi, K., Coutanceau, M., Daube, O., Loc, T.P., 1991. Further experiments on vortex formation around an oscillating and translating airfoil at large incidences. Journal of Fluid Mechanics 225, 607–630.

Scanlan, R.H., 2000. Motion-related body-force function in two-dimensional low speed flow. Journal of Fluids and Structures 14, 49–63.

Scanlan, R.H., Jones, N.P., 1999. A form of aerodynamics admittance for use in bridge aeroelastic analysis. Journal of Fluids and Structures 13, 1017–1027.

Scanlan, R.H., Tomko, J.J., 1971. Airfoil and bridge deck flutter derivatives. ASCE Journal of the Engineering Mechanics Division 97, 1717–1737.

Shen, W.Z., Ta Phuoc, L., 1995. Simulation of 2D external flows by means of decomposition method using an influence matrix technique. International Journal for Numerical Methods in Fluid 20, 111–1135.

Tamura, T., Ohta, I., Kuwahara, K., 1990. On the reliability of the two-dimensional simulation for unsteady flows around cylinder-type structure. Journal of Wind Engineering and Industrial Aerodynamics 35, 275–298.

Theodorsen, T., 1931. Theory of wing sections of arbitrary shape. NACA Technical Report 411.

Vanel, J.M., Peyret, R., Bontoux, P., 1986. A pseudospectral solution of vorticity-streamfunction equations using the influence matrix technique. In: Morton, K.W., Baines, M.J. (Eds.), Numerical Methods for Fluid Dynamics. Clarendon Press, Oxford, pp. 463–475.

Worlibar, A.S., Knio, O.M., Klein, R., 1998. Numerical simulation of the thermoaccoustic refrigerator: II Stratified Flow around the Stack. Journal of Computational Physics 144, 299–324.

Zang, J., Dalton, C., 1997. Interaction of a steady approach flow and a circular cylinder undergoing forced oscillations. ASME Journal of Fluids Engineering 119 (4), 808–813.

Zienkiewicz, O.C., 1977. The Finite Element Method in Engineering Science, 3rd Edition. Mc Graw-Hill, New York.